UNIVERSITY OF OKLAHOMA

GRADUATE COLLEGE

DOPANTS AND SURFACE EFFECTS ON Mo-BASED BIFUNCTIONAL CATALYST FOR METHANE DECOMPOSITION

A THESIS

SUBMITTED TO THE GRADUATE FACULTY

in partial fulfillment of the requirements for the

Degree of

MASTER OF SCIENCE

By

EYMI LAYZA ESCOBAR

Norman, Oklahoma

2026

DOPANTS AND SURFACE EFFECTS ON Mo-BASED BIFUNCTIONAL CATALYST FOR METHANE DECOMPOSITION

A THESIS APPROVED FOR THE

SCHOOL OF SUSTAINABLE CHEMICAL, BIOLOGICAL AND MATERIALS ENGINEERING

BY THE COMMITTEE CONSISTING OF

Dr. Steven Crossley, Chair

Dr. Dimitrios Papavassiliou

Dr. Lance Lobban

Table of Contents

Acknowledgements vi

List of Figures viii

Abstract x

Chapter 1: Introduction 1

CNTs growth mechanism 2

Bifunctional catalyst 4

Metal-Support interactions 4

Molybdenum addition and CNTs properties 5

Dopants effect on catalyst dynamics 7

Research scope 9

Chapter 2: Experimental set up 10

2.1. Catalyst preparation 10

2.2. Evaluation of catalytic performance & CNT synthesis 11

2.3. Catalyst and CNTs characterization 12

Chapter 3: Results and discussion 14

3.1. Dopants addition and their preparation method 14

3.2. Metal surface exposure for dopant deposition 17

3.3. IWI treated catalyst and its water-induced metal exsolution 19

3.4. Surface changes upon water-induced metal exposure 25

3.5. Evaluation of carbon products 29

3.6. Mechanistic insight into water-induced metal exposure 31

Chapter 4: Concluding remarks 33

Appendix A: Supporting information 39

Acknowledgements

To my parents Helen, Segundo and Cariñona for giving me so much love, happiness and support. They envisioned the way of accomplishing my dreams, always believing in me. I came here because of the values instilled in me and all their life teachings. I do not know what I would do without my family, and I appreciate everything they have done for me.

My advisor Dr. Steven Crossley, who provided an endless amount of support, positivity, and guidance throughout my time in graduate school. He spent an enormous amount of time discussing research with me and promoting my professional skills. He provided me with the opportunity to come to OU. He opened a space for me in his investigation group to boost my learning and deep understanding to become an excellent researcher as he is. I consider myself lucky to be guided by such an incredible professional. His encouragement and enthusiasm helped me all the time in this process. Also, many thanks to Dr. Lobban, Dr. Resasco, and Dr. Papavassiliou for always being open to help, answering my questions, collaborating, and involving me in many academic activities.

Dr. Maqque and Dr. Aguilar for giving me the opportunity to live and study at the University of Oklahoma. They believed in me even before I came, they recognized my potential and connected me with many opportunities. Thanks to them, I am now making a dream come true by achieving my Master's degree.

Eduardo, thanks for being next to me on each step of my journey. Thank you for being the light in the darkest days. I am lucky to count on someone so kind, lovely and intelligent like you.

Additionally, I would like to thank my colleagues in Dr. Crossley's group. Thank you for being helpful, friendly, and kind despite the routine. All of them are always willing to help with lab troubles. They were great resources to bounce ideas off before completing this thesis. Special thanks to Ranuja, Caleb and Phuong for helping me in any way we found possible and sharing this process of learning and growing with me, the best of luck for them in their future endeavors.

I would also like to extend my gratitude to SCBME department at OU for allowing me to pursue my master's degree. Special thanks go to SCBME department staff for their assistance.

List of Figures

Figure 1. Product cost and CO_2 footprint of hydrogen production technologies [3]. 2

Figure 2. Mechanism of the formation of filamentous carbon [6]. 3

Figure 3. Effect of metal-support interactions on CNTs yield from CH4 at 900°C [12]. 5

Figure 4. Effect of Mo loading on 4%wt Fe/MgO: carbon productivity (in 30 min, red column) and graphitization (blue square) of different catalysts. The carbon graphitization is D/G ration of the Raman spectra [26]. 6

Figure 5. Effect of Gd addition in the interface Fe - Al substrate. Initial growth rate and the growth lifetime of 0.5 and 1 nm layer of Iron [41]. 8

Figure 6. Reactor set up diagram. 11

Figure 7. Influence of dopant-addition method for NiMo/MgO catalyst synthesis. Reaction during 3 hours at 800°C. 14

Figure 8. Effects of dopant loading in doped NiMo/MgO by IWI method on carbon yield after 3 hours of CMD at 800°C. 15

Figure 9. H_2 evolution rate profiles of dopants added by IWI compared to base catalyst. 1 atm, TOS: 3h, 800°C. 16

Figure 10. A) Carbon yields of 3 hours run, B) Rate profiles based on H2 evolution at 800°C. 17

Figure 11. Initial growth rate and decay constant based on rate profiles..... 18

Figure 12. Temperature dependence of initial rates in the range of 800 - 725°C of base, water-treated and Gd-doped NiMo/MgO catalyst. 19

Figure 13. SEM images of base and treated catalyst with BET surface area measurement.20

Figure 14. High resolution XRD in the MgMoO4 region of base NiMo/MgO comparison with treatment and Gd addition. 21

Figure 15. H_2 evolution rate profiles comparison of NiMo/MgO base treated with water after 1 calcination, 2 consecutive calcinations, and water addition between 2 calcinations. 22

Figure 16. Gd and water addition treatment in prepared catalysts at each stage of NiMo/MgO species evolution. A) Rate evolution of fresh treated catalyst. B) Rate evolution of reduced treated catalyst. C) Rate evolution of carburized treated catalyst. 23

Figure 17. Elemental composition based on high resolution XPS of Ni and Mo content on the surface during catalyst evolution of NiMo/MgO. 25

Figure 18. Oxidation states of Ni $2p_{3/2}$ and Mo $3d_{5/2}$ evolution after calcination, reduction and carburization for base and treated NiMo/MgO. 26

Figure 19. XPS spectra of region Ni $2p_{3/2}$ in fresh catalyst. 27

Figure 20. Region Mo 3d of carburized catalyst; for base and treated catalyst..... 28

Figure 21. Raman analysis of CNTs. a) D/G ratio analyzed with t test in treated catalyst respect to the base, b) D and G bands of base and treated CNTs, c) D/G ratios at 30 min and 3 hours of time on stream. 30

Figure 22. CNTs diameter distribution and HR-TEM images produced from base and water treated NiMo/MgO at 800°C. 31

Figure 23. Schematic of (A) formation of Ni nanoparticles clusters during IWI treatment, and (B) carburization and Ni exsolution mechanism upon methane introduction..... 32

Abstract

Specialized catalysts are required for high-yield carbon nanotube (CNT) and hydrogen production from catalytic methane decomposition (CMD). Developing upgraded NiMo/MgO catalysts necessitates understanding of the dynamics of metal evolution and CNT growth. Here we evaluate the potential of several dopants (Gd, Ga, Bi, La) over NiMo/MgO and establish a new water-induced metal exposure method in the catalyst preparation to boost methane activation and produce base growth CNTs. Catalysts doped with 0.2wt% Gd by incipient wet impregnation (IWI) showed higher carbon yields than other dopants. However, the method of dopant introduction impacted measured rates significantly after comparative analysis. It was determined that NiMo/MgO post-treatment, comprising of a water washing step and a second calcination, facilitated metal exposure that increased 30% of the initial catalyst activity. Upon treatment, carbon yields increased from 12.5 g_C/g_{cat} to 14.3 g_C/g_{cat}, generating a narrower CNT diameter distribution and more graphitic carbon after 3 hours on stream. Gd doping by this method showed a modest 5% increase on rate enhancement. Characterization by BET, XPS, XRD, TEM, and Raman revealed that water induced metal exposure increases the availability of Ni active sites on the surface by displacing Mo species during washing. Graphitic quality of CNTs increased by 10%, and average diameter shrank by 35%. Ni/Mo ratios were found to impact catalytic activity more than dopant addition. This work reveals an effective dopant impregnation method in catalyst preparation and provides insights into CNT growth understanding via surface phase interactions of treated and standard NiMo/MgO, demonstrating a synergistic effect between metal exposure and dopant addition.

Chapter 1: Introduction

In 2024, global gas flaring emitted 151 billion cubic meters of gases composed of methane mainly; putting into the atmosphere the equivalent of 400 million tons of carbon dioxide [1]. This fact points out the need for methane capture, where gas and oil regions pose key roles in reducing emissions with widely known processes and facilities that could help decarbonize the industry at affordable costs.

Catalytic methane decomposition (CMD) is a promising technology to implement, offering potential benefits such as CO_2-free hydrogen production (**Figure 1**) and advanced carbon materials, including CNTs, all in a single reaction. Its major drawback lies in high-temperature requirements, catalyst deactivation, and reactor system clogging caused by solid carbon formation. Even though solid carbon limits CMD great scaling, promoting ordered growth of CNTs over specialized catalysts can prevent deactivation, prolonging the life of active sites in the catalyst. Thus, engineered catalysts could achieve stable CNT growth by modifying the rate of methane deposition relative to the rates of carbon diffusion across the metal lattices, enhancing CNTs nucleation mechanisms [2].

The conversion of methane to hydrogen and CNTs through catalytic pyrolysis presents great economic potential over alternative methods. However, the deep understanding of nucleation and growth conditions at the surface of growing nanotubes, the conditions which control microstructure, length and spatial ordering of nanotubes are still not well understood.

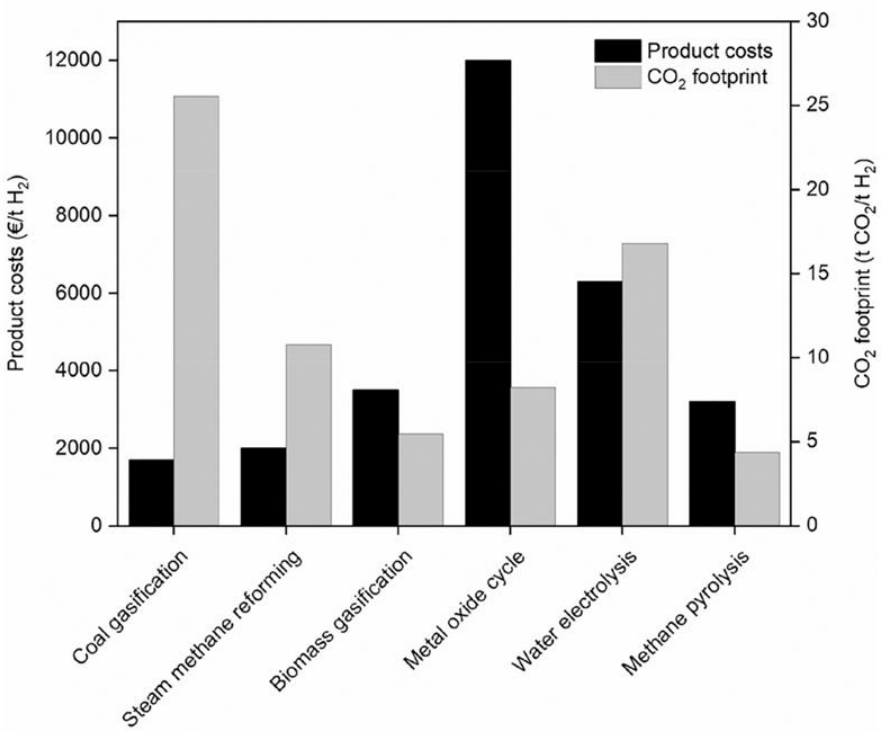

Figure 1. Product cost and CO_2 footprint of hydrogen production technologies [3].

Some authors agree that the reaction mechanism for methane decomposition involves the molecular adsorption of CH_4, where methane is first adsorbed on the catalyst surface and then dissociates following a series of stepwise surface dehydrogenation reactions [4]. In this sense, the rate-limiting step of the decomposition is the abstraction of the first hydrogen atom from adsorbed methane to form an adsorbed methyl group. On the other hand, dissociative adsorption models agree that methane dissociates upon adsorption on the catalytic active sites generating chemisorbed CH_3 and H fragments, following further dehydrogenation [3].

CNTs growth mechanism

Since catalysts for carbon nanotubes production are prone to encapsulation, the hydrocarbon activation plays a key role on CNTs growth, where graphitic carbon formation is energetically more favorable than nanotube construction [5]. The formation of carbon filaments from

hydrocarbons on Ni crystallites, as shown in **Figure 2**, proceeds via (a) methane adsorption [4]/ dissociative chemisorption on metal surfaces to form carbon atoms, (b) the dissolution of carbon atoms into the metal, (c) the bulk diffusion of the carbon atoms through the metal, and (d) the nucleation of filaments and the precipitation of carbon atoms at the metal− filament interface at the location on the crystallite surface where filament nucleation initially occurred. The rate of filament growth on surface active sites is limited by the rate of carbon diffusion through metal particles such as Ni, Fe and Co [2].

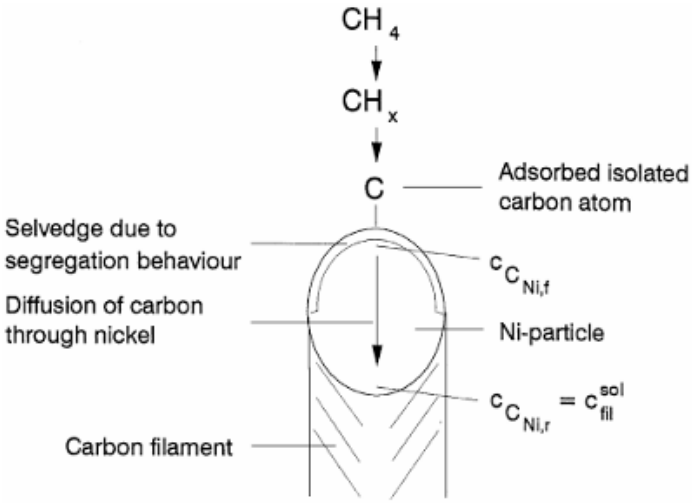

Figure 2. Mechanism of the formation of filamentous carbon [6].

The kinetic models for double- and single-walled carbon nanotube synthesis are based on the presence of only one type of active sites, whereas that developed for the formation of multiwalled carbon nanotubes considers two different types of active sites. Here, CH_x* and H* species are adsorbed on different kinds of active sites [3].

Bifunctional catalyst

Common catalyst formulations focus on promoting C-H scission of methane for further nucleation into CNTs, involving active metals such as Ni, Fe, and Co [3]. From them, Ni has been shown to facilitate hydrocarbon dissociation at mild temperatures (500-800°C), producing high yields and promoting stability over time for CNT and H_2 production [7-9]. Since Ni has partially filled 3d orbital, this facilitates the CH dissociation of the hydrocarbon molecules through partially accepting electrons. This interaction along with the "back donation" from the metal into the unoccupied orbital in the hydrocarbon molecule changes the electronic structure of the adsorbed molecule so the dissociation occurs [7]. This performance is often associated with MgO as support, which prevents sintering and attributes high surface area and lasting temperature stability [10, 11].

Metal-Support interactions

The metal–support interaction is believed to play important roles in nanotube growth as its yield strongly depends on the support material. In this sense, Fe/Mo particles on alumina (Al_2O_3) produced a much higher amount of SWCNTs than those grown on silica (SiO_2) as shown in **Figure 3** [12]. This was attributed to the stronger metal–support interaction for the Al_2O_3 support than that for SiO_2 [13].

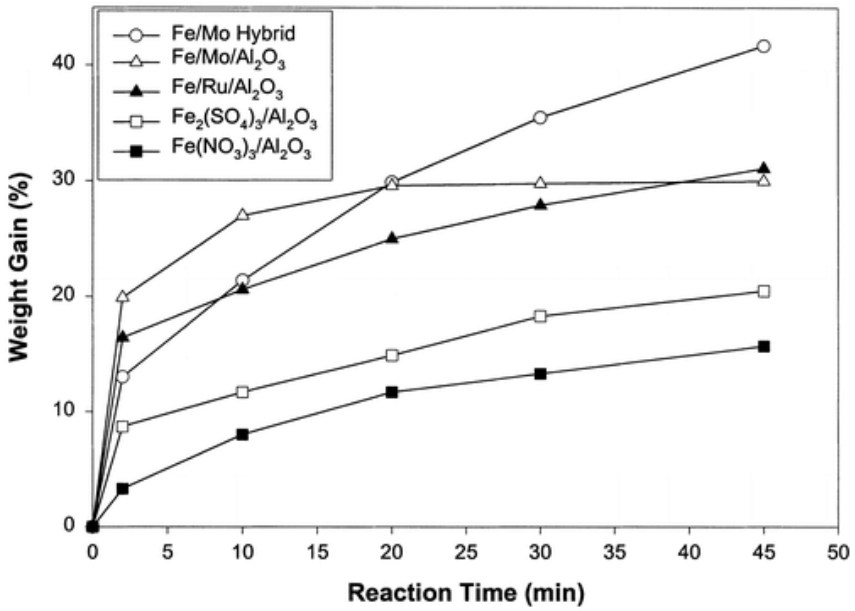

Figure 3. Effect of metal-support interactions on CNTs yield from CH4 at 900°C [12].

MgO is an attractive support material from the view of a large-scale synthesis of SWCNTs and double-walled carbon nanotubes because the supported catalysts give high-quality nanotubes and MgO can be removed by a relatively mild acidic treatment [13]. The metal–support interaction has been studied by using flat substrates such as Si, SiO_2, and crystals of sapphire (Al_2O_3) and MgO as model systems [13]. These studies have also shown that the support material significantly influences the catalytic activity of metal catalysts, suggesting the importance of the metal–support–substrate interactions.

Molybdenum addition and CNTs properties

Metal-Mo-MgO systems evolve with reaction conditions, where catalytic sites for CH_4 activation are suggested to be finely dispersed Mo particles or Mo-carbides (or oxycarbides) formed in situ from the unreduced Mo-oxide component [14]. The addition of molybdenum modifier to Fe [15] or Co[16] can be beneficial, but the effect depends – among others – on the

Mo content. For example, the use of CoMo/MgO catalyst with high Mo content was not favorable for the production of high-quality carbon nanotubes, but in another case the improvement of thermal stability of the catalyst and graphitization degree of MWCNTs was detected upon addition of 25% Mo to a 25% Co/MgO catalyst [14, 17].

As a promoter, Mo addition has been proved to boost activity of Ni, Fe, and Co supported on MgO [18-20], exhibiting synergistic effects through enhanced metal dispersion and strong metal-support interactions (SMSI), as well as its ease of forming alloys with active metals and MgO [17, 21-24]. Understanding of the Mo evolution and its interactions in metal-Mo-MgO systems is key to improve CNT production, since varying the Mo loading can tune CNT properties, such as wall number, diameter, graphitization (**Figure 4**), and chiral quality [18, 25, 26].

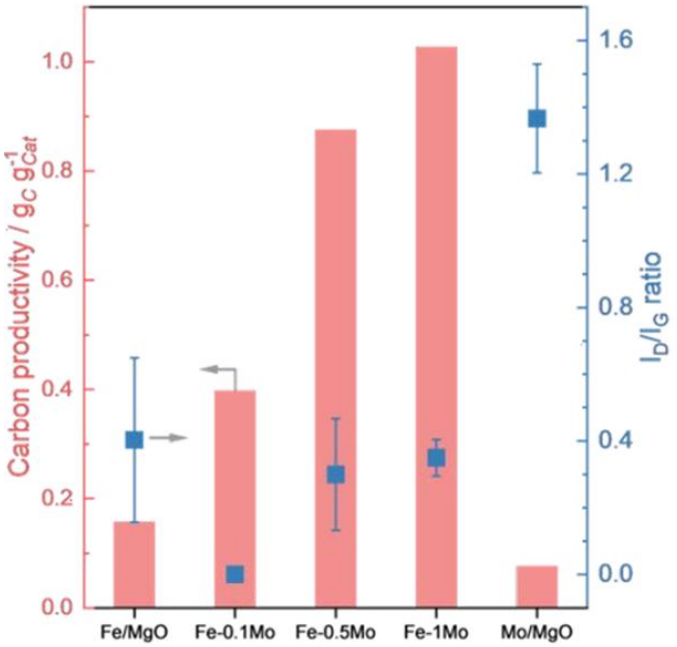

Figure 4. Effect of Mo loading on 4%wt Fe/MgO: carbon productivity (in 30 min, red column) and graphitization (blue square) of different catalysts. The carbon graphitization is D/G ration of the Raman spectra [26].

Recently, Gomez et al. [20] delved into the surface dynamics of NiMo/MgO for CH_4 activation and base-growth CNTs. Species including $MgMoO_4$, MoO_{3-x}, and Mo_2C were found to evolve as part of the surface change at high temperatures, and an exsolution of Ni nanoparticles during carburization was found to govern the nucleation of CNTs. $MgMoO_4$ species distribute Mo creating higher density of nucleation sites, and can also activate CH_4 at 1000°C [21].

Dopants effect on catalyst dynamics

Due to the complexity of metal-Mo-MgO catalysts, the addition of dopants and their effects on methane activation and CNT production remain unexplored. Dopant addition is known to modify catalytic activity via electronic effects, modifying the strength of binding energies, and via geometric effects, through changes on coordination number or atomic arrangement [27]. Through these effects, molten-metal-like dopants exhibit clear modifications in catalyst-adsorbate interactions, boosting stability and selectivity, e.g., Pt doped with Ga or Sn [28-30]. On nickel, molten Pb enhances reaction rates [31], while Ga disrupts CNTs formation during dry methane reforming [32]. The disruption of metal-Mo interactions over SiO_2 for CNTs production was studied on cobalt doped with sodium, which led to strong hindering effects on metal-Mo phase formation [33].

In comparison, rare earth metals like La, Gd, and Y also exhibit geometric effects in methane activation due to their ionic radius [34] and electronic effects related to basicity [35-38]. Among lanthanides, doped gadolinium has been shown to promote supergrowth of cm-long CNTs over iron catalysts using ethylene, as well as a higher growth rates, **Figure 5** [39, 40]. Sugime et al. [41] found that Gd prevents Fe migration into the lattice of Al_2O_x support via disruption of strong metal-support interactions (SMSI) and suppresses iron carbide formation, promoting ordered CNT

forests. Moreover, dopants effects are surface-dependent, and strongly affected by their introduction method [42].

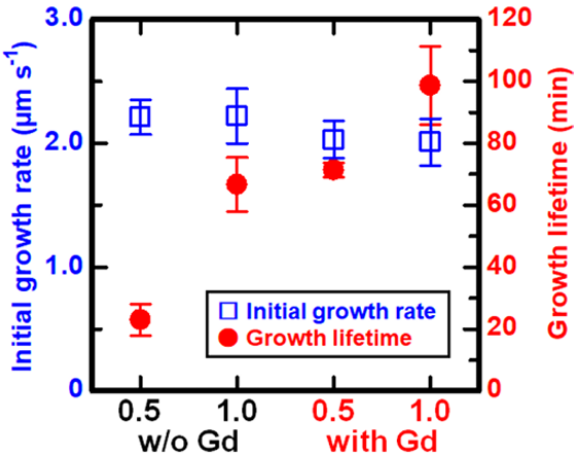

Figure 5. Effect of Gd addition in the interface Fe - Al substrate. Initial growth rate and the growth lifetime of 0.5 and 1 nm layer of Iron [41].

The dopant-addition process in supported bimetallic catalyst mixtures can be complex, since different addition methods can locate dopants across radial gradients between surfaces and bulk structures [42]. The impact of dopants becomes more convoluted on complex and dynamic catalysts like the NiMo/MgO catalyst, with Ni exsolution processes happening around 800°C [20]. Thus, incipient wetness impregnation (IWI) is a common method in dopant addition that introduces dissolved metal salts into a solid base, aiming for good dispersion. In IWI method, the use of solvents is essential, and its interaction with the solid base can dictate the location of the metal added. Several authors have reported that MgO is partially soluble in water [25, 43], and solvents could affect MgO interactions with dopant [44, 45]. In this sense, the IWI method with water addition could rearrange Ni, Mo and Mg interactions on NiMo/MgO catalyst.

Research scope

Here, we evaluate the effects of molten-metal-like dopants and rare earth metal dopants, especially Gd, on the NiMo/MgO catalyst for CH_4 pyrolysis. The impact of each dopant was assessed through two methods of introduction: coprecipitation and incipient wetness impregnation (IWI). Gd was found to promote higher catalytic activity among tested dopants. Some of this boosted activity was found to result from the method of dopant introduction, leading to an enhanced preparation method for doped Ni-Mo-MgO catalysts. The new catalyst treatment relies on partial $MgMoO_4$ solubility and mobility in water to rearrange the catalyst surface after synthesis and was proved to expose additional active Ni from the bulk lattice by XPS, while keeping its crystalline structure. The water-induced metal exposure treatment results in 30% boost in initial CMP activity. Rate profiles of H_2 evolution were the main kinetic descriptors, while deactivation constant (k_d), temperature-dependence, and DFT calculations unravel the changes in surface adsorbate- catalyst interactions. Upon water-induced metal exposure, produced CNTs showed 10% increase on graphitic quality on Raman, and up to 35% shrinkage on diameter distribution assessed by TEM. The water-induced metal exposure treatment exhibited a synergistic effect exists between Gd and Ni in the Gd-doped NiMo/MgO catalyst. These results reveal a new strategy for catalyst design and provide insights into the understanding of SMSI during Ni-Mo-MgO evolution and its effects on CNT growth toward efficient CMD activation and high-yield CNT production.

Chapter 2: Experimental set up

2.1. Catalyst preparation

The standard NiMo/MgO catalyst (5 wt% of Ni and 25 wt% of Mo, molar ratio: Ni/Mo=0.33) was prepared via partial co-precipitation of Mo and Ni precursors salts over MgO powder. Ammonium molybdate ($(NH_4)_2MoO_4$, > 99.99%, ThermoFisher Scientific Co., Ltd.), nickel (II) nitrate hexahydrate ($Ni(NO_3)_2{\cdot}6H_2O$, >98%, Alfa Aesar Co., Ltd.), and magnesium oxide heavy powder (MgO, >98%, Spectrum Chemical Co., Ltd.) were used as precursors for standard catalyst synthesis. Dopants precursors were gadolinium (III) nitrate hexahydrate ($Gd(NO_3)_3{\cdot}6H_2O$, >99.9%) and lanthanum (III) nitrate hexahydrate ($La(NO_3)_3{\cdot}6H_2O$, >99.99%) were purchased from Sigma Aldrich Co., Ltd. Gallium (III) nitrate hydrate ($Ga(NO_3)_3{\cdot}xH_2O$, >99.9%) and bismuth (III) nitrate pentahydrate ($Bi(NO_3)_3{\cdot}5H_2O$, ≥98.0%) were purchased from ThermoFisher Scientific Co., Ltd. Ammonium molybdate salt (1.1 g) was first dissolved in 20 mL of deionized water in a beaker submerged in a water bath at 60°C on a hot plate; then, 0.5 g of nickel (II) nitrate hexahydrate was added to the solution.

Upon complete dissolution, 2 g of magnesium oxide were added and the mix started stirring at 600 rpm while water bath temperature was set to 90°C until complete water evaporation. The mixture was cooled to room temperature to be transferred to a ceramic dish and dried under vacuum for 24 hours. The dried sample was passed through a No. 80 sieve (180 μm) and then calcined at 600°C in 100 sccm of air flow for 3 hours with a ramp of 10°C min^{-1}.

In the doping process, coprecipitated dopants were added along with Mo and Ni salts. For incipient wet impregnated dopant process, each dopant salt precursor amount (calculated based on metal wt%) was dissolved in 1.5 mL of deionized water. The solution was added by drop-casting

with a pipette onto the base NiMo/MgO catalyst while manually stirring until wet impregnation was reached. The amount of dopant metal loading (0.1, 0.2, 0.5, 1 and 2 wt%) was made based on 2g of MgO. After the dopant impregnation, the catalyst was dried under vacuum for 24 hours and sieved to 180µm. A second calcination was employed at 600°C in 100 sccm of air flow for 3 hours to remove precursors and water.

Deionized water with conductivity of 0.4 µS/cm, and ethanol grade ACS from Sigma Aldrich Co., Ltd were employed. A custom-built system, maintained under a nitrogen-controlled environment, was used to isolate and store the catalysts (fresh catalysts) from ambient conditions and prevent air exposure.

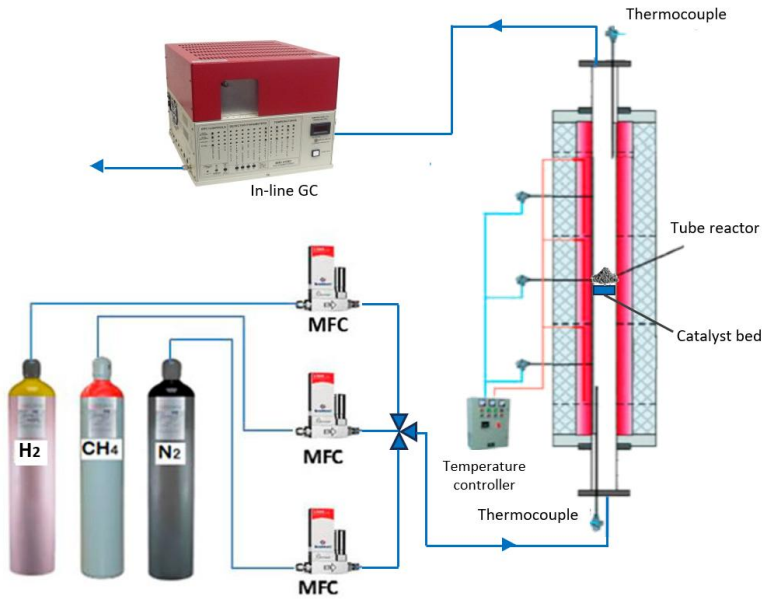

Figure 6. Reactor set up diagram.

2.2. Evaluation of catalytic performance & CNT synthesis

The CMD experiments were carried out in a continuous fixed-bed reaction system, **Figure 6**, with a quartz tube of an inner diameter of 11 mm and a length of 61 cm. Sintered quartz sand bed was located at the isothermal region of the reactor tube and loaded with 10 mg of fresh catalyst.

The sample was heated at 10°C/min to 650°C and *in-situ* reduced under H_2 flow rate of 30 sccm by 30 min [20]. After reduction, nitrogen was introduced, and the reactor was heated to 750–800°C. Subsequently, methane was continuously introduced for 0.5-3 hours for catalytic pyrolysis. N_2 and CH_4 were introduced at flow rates of 30 sccm.

The process had a vertical upward flow. The assessment of catalytic performance was based on the hydrogen produced up to 3 h. Methane and hydrogen evolution were tracked by an SRI-8610C gas chromatograph fitted with MS5A and HaysepD columns and equipped with thermal conductivity (TCD) and flame ionization (FID) detectors. As the reactor cooled to room temperature, nitrogen was used as an inert gas.

The carbon and CNTs accumulated in the reactor tube frit were collected post reaction. Carbon produced and the carbon yields were calculated based on the mass obtained after the reaction and the mass of the catalyst used for the reaction. The hydrogen signal obtained in the mass balance was calibrated each run based on the amount of carbon accumulated on the catalyst.

2.3. Catalyst and CNTs characterization

X-ray diffraction (XRD) analysis was carried out on a Rigaku Ultima IV diffractometer with Cu Kα radiation (λ =1.5405 Å) operating at 40 kV and 44 mA. Continuous scan mode was employed, recording diffraction data at a scanning speed of 1.0°(2θ) per minute.

Scanning electron microscopy (SEM) analysis was performed on a Zeiss Neon Microscope using conductive carbon tape. Energy-dispersive X-ray spectroscopy (EDS) was additionally utilized for mapping and quantifying elements at 20kV.

Nitrogen adsorption isotherms were measured at 77 K using Micromeritics ASAP 2460. Before testing, 500 mg of each catalyst were degassed at 175ºC under vacuum for 5 h. BET surface areas were calculated using isotherm data in the $0.05 < P/P0 < 0.4$ relative pressure range.

X-ray photoelectron spectroscopy (XPS) for surface analysis was conducted by a Thermo scientific ESCALAB 250Xi equipped with an Al Kα X-ray source at 10 kV and 10 mA. Samples were handled inside a dry box under nitrogen and degassed before analysis. Binding energy values were calibrated based on C (1s) peak at 284.8 eV, then Shirley background was applied.

Raman spectra were collected at room temperature using a Renishaw InVia mapping Raman microscope with a 532 nm green laser set to 5%. The data analysis was conducted using Wire 4.1 software. The data was normalized, and peak areas were obtained using Origin after performing normalization, baseline correction and curve fitting of each spectrum.

High-resolution transmission electron microscopy (HRTEM) was performed using a JEOL 2010 field-emission S/TEM operated at 200 kV with a DE-12 direct electron camera. The diameter of CNTs for all the samples was imaged 300 mesh copper lacy carbon grids. These samples were prepared by sonicating the CNTs in ethanol for 10 minutes and drop-casting 5 µl onto the lacy carbon-coated copper grids. Raw images were Fourier-filtered to remove camera noise and enhance contrast.

Chapter 3: Results and discussion

3.1. Dopants addition and their preparation method

The introduction of a dopant to a catalyst aims to disrupt its surface by modifying metal-support interactions, influencing rates on CMP. Dopants studied on NiMo/MgO catalysts were molten metals with low melting points: bismuth and gallium; and rare earth metals: gadolinium and lanthanum. Dopants were introduced by two methods of preparation: coprecipitation (CP) and incipient wetness impregnation (IWI). For CP, the dopant salt was added along with Ni and Mo precursors over MgO powder; while for IWI, the dopant precursor was added over fresh NiMo/MgO catalyst and sequentially calcined (see methods). **Figure 7** shows the performance of each dopant according to its introduction method in turn to carbon production. The IWI method displayed higher carbon yields than CP for comparable dopant loadings.

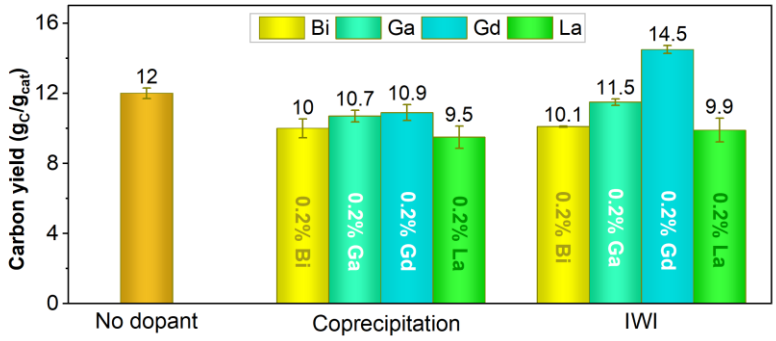

Figure 7. Influence of dopant-addition method for NiMo/MgO catalyst synthesis. Reaction during 3 hours at 800°C.

Wetness impregnation methods can promote the metal precursor to adsorb in an eggshell distribution in which much of the dopant is found on the catalyst surface [46], while coprecipitation could render some of the dopant inaccessible in the bulk structure of the catalyst. Therefore, the superior performance of IWI compared to CP is expected, and IWI was further evaluated. In IWI

process, a dopant trend was more noticeable, where Ga outperformed Bi among molten metals, while Gd surpassed La dopants in yields. Gd added by IWI increased the carbon yield by 21% over the undoped NiMo/MgO catalyst. **Figure 8** shows the carbon yields for higher wt% dopant loadings. Loadings of 0.5 wt% were found to be ideal for molten metals, while 0.2 wt% worked best for lanthanides. Dopant loadings greater than 2% decreased the activity. Ga performed better than Bi, whilst La had lower activity than Gd. A 0.2 wt% Gd load showed the highest performance with 14.5 g carbon per gram of catalyst after 3 hours of reaction. The trend in carbon yield was comparable in 30 minutes time on stream (TOS), and 0.1% Gd loading did not enhance the carbon yield further (Fig. S1).

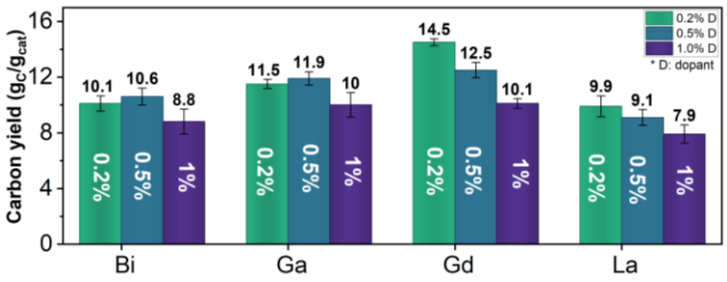

Figure 8. Effects of dopant loading in doped NiMo/MgO by IWI method on carbon yield after 3 hours of CMD at 800°C.

For further insights into the role of dopants, rate profiles based on H_2 evolution were tested in **Figure 9** for best loadings of Ga, Gd and La. Measured rates describe NiMo/MgO catalyst evolution: catalyst carburization, activation step, and fast and slow deactivation due to solid carbon production. Carburization and catalyst activation by Ni exsolution precede carbon nucleation and CNT growth, and it is observed as an initial steep increase in H_2 production related to base growth CNTs [20, 22]. The rate profiles of doped catalysts capture differences in carburization and activation steps (maximum rate and slopes) by the first 30 minutes of reaction, that describe the influence of dopants to create variations in deactivation profiles.

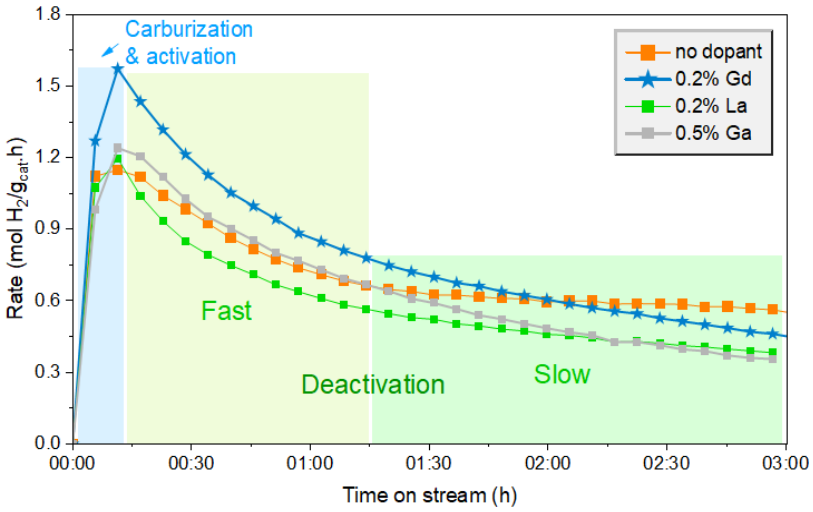

Figure 9. H_2 evolution rate profiles of dopants added by IWI compared to base catalyst. 1 atm, TOS: 3h, 800°C.

In general, deactivation was more pronounced for doped catalysts than the base catalyst, which is associated with the catalyst surface disruption that dopants produce on carbon growth. Rate profiles evidence that low loading of dopants can affect the nature of SMSI between Ni, Mo and Mg for further change in the reaction steps. Gd doped NiMo/MgO showed a 30% up to 2 hours on stream. Similar trends are shown with 0.1 wt% Gd loading (Fig. S2a). A steeper slope to the maximum rate could imply faster carburization and catalyst activation with subsequent change in carbon nucleation and growth; however, it also showed stronger deactivation. Other works reported that low loadings of Gd added by metal deposition between metal and support enhances CNT yields by enhancing active metal dispersion [39, 41].

La-doped catalyst showed comparable spike and fast deactivation profiles as Gd but with lower performance. Ga exhibited comparable rates as the base catalyst until 1.5 hours TOS, after which Ga also promoted further deactivation affecting the total carbon yield. Bumped profile of 0.5 wt% of molten Ga at 800°C could be related to a disrupted surface carbon formation, promoting

slower catalyst activation stages. Further deactivation after 1 hour is more related to addition method as explained in next section.

3.2. Metal surface exposure for dopant deposition

Gd showed a promising role among tested dopants, improving H_2 production of the base catalyst for the first 2 hours. However, further testing indicated that the IWI treatment of NiMo/MgO with water and no dopant precursor salt addition can produce comparable high carbon yields. Water could alter the surface structure of NiMo/MgO system during the wetness impregnation, and a second calcination would restructure the metal species interactions.

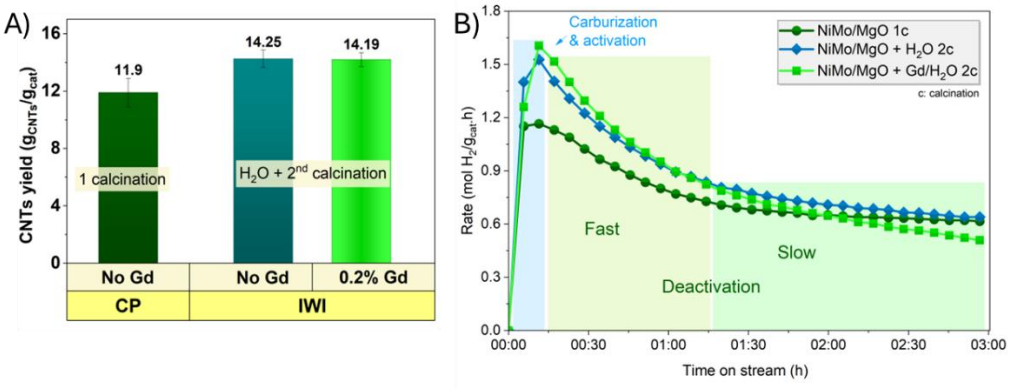

Figure 10. A) Carbon yields of 3 hours run, B) Rate profiles based on H2 evolution at 800°C.

Figure 10A illustrates the comparison on carbon yields of the base catalyst with and without treatment. Treated base boosted the total conversion by 19% with respect to untreated catalyst, solely by introducing water to the catalyst. The observed yield increase resulting from water introduction is comparable with yields of Gd doped catalyst. This implies that the apparent rate enhancement of Gd dopant is primarily due to water addition and a second calcination treatment. Rate profiles based on H_2 production for treated catalysts are analyzed in **Figure 10B**.

Treated catalysts show that much of the increase of activity results from IWI treatment with water, though the presence of Gd does appear as a modest rate increment. Carbon accumulations were consistent with observed trends (Fig. S3). Based on rate profiles, **Figure 11** illustrates the initial growth rate boosts of 31 and 38% on catalyst activation-carburization steps with water treatment and Gd addition, respectively. Gd addition represents an effective 5% boost over treated base.

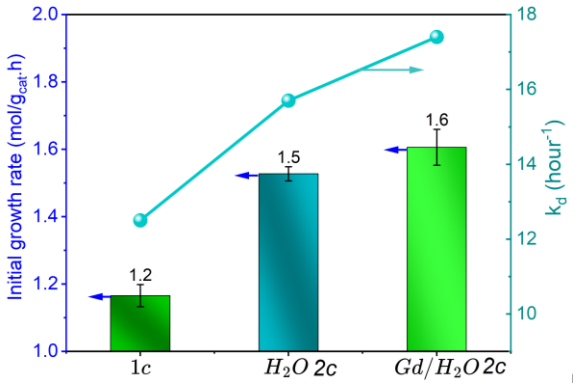

Figure 11. Initial growth rate and decay constant based on rate profiles.

The boost of water treatment and Gd-slight increase are consistent even at lower temperatures of reaction as shown in **Figure 12** and Fig. S4. However, higher initial rates come along with rapid time-dependent decay, **Figure 11**. Measured deactivation constants (k_d) were greater for Gd-doped catalysts, followed by water treated and base catalysts, where the possible main deactivation mechanism is the encapsulation of active sites.

Fast deactivation periods depict the strong activity decay due to sites loss as carbon evolves and deposits; in this period, the bed turns into an expanding bed where the catalyst loses surface area for methane activation. Slow deactivation periods depict the remaining activity of fewer active sites resisting caping. We hypothesize that the water treatment could facilitate the redistribution of the surface structure, as we will show in section 3.3, possibly creating smaller nanoparticles and

promoting lower coordination number, while Gd addition promotes methane activation and carbon production. Even when different groups have reported Gd to promote better CNT growth [40, 41, 47], the beneficial impact of Gd in particulate catalysts seems less noticeable and surpassed by water and Mo effects on Ni dispersion. Thus, the slight rate increase with Gd dopant could suggest a promotion of Gd-Ni interactions in the surface produced by the IWI treatment, since an outer Gd position was demonstrated to improve CNTs growth as the sub monolayer below on Fe over Al_2O_x [41]. Further experiments showed that the impact of Gd was minimal regardless of the wt% loading or method of introduction (Fig. S2).

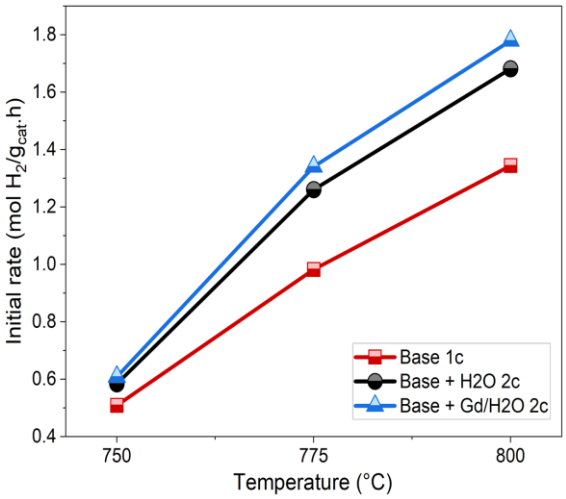

Figure 12. Temperature dependence of initial rates in the range of 800 - 725°C of base, water-treated and Gd-doped NiMo/MgO catalyst.

3.3. IWI treated catalyst and its water-induced metal exsolution

The water-washed catalyst was characterized to investigate its effect promoting CMP on NiMo/MgO. SEM images in **Figure 13** illustrate how the wetness impregnation treatment produces agglomerated particles, changing the catalyst particle morphology. The agglomeration is attributed to MgO partial solubility with water, reacting to form brucite ($Mg(OH)_2$), which

generally forms a weak and porous structure with volumetric expansion [43]. This implies that high surface areas would be expected; however, BET analysis reveals that the surface area of the water-washed catalyst only increased by 4%.

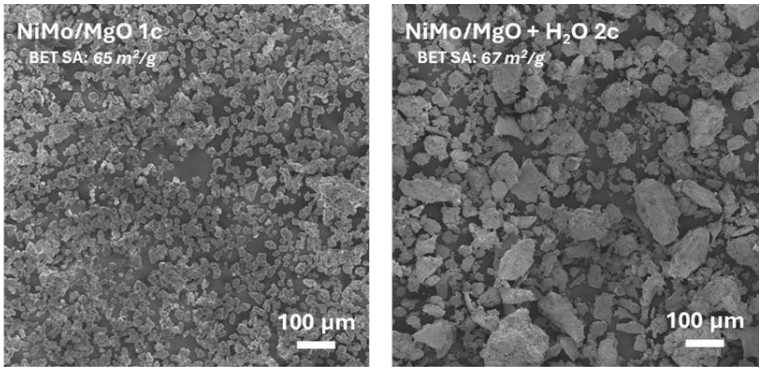

Figure 13. SEM images of base and treated catalyst with BET surface area measurement.

To test structural changes after the second calcination, XRD analysis was conducted in Fig. S6, identifying same characteristic MgO and $MgMoO_x$ alloy spectrum. **Figure 14** focuses on higher resolution over the alloy region, where $MgMoO_4$, MoO_2 and $MgMo_2O_7$ species were identified. IWI-treated NiMo/MgO exhibit no changes in crystal sizes and species (Table S1). This observation implies that the aggregates formed in IWI treated catalysts have similar bulk structure than untreated catalysts, no separation of Mg and Mo oxides occur after a second calcination, and the improvements in rate must be attributed to take place in the catalyst surface. Moreover, Gd crystallites were too small for detection via XRD (at 0.2 wt%), EDS (Fig. S7), and no changes were noticed in the Gd-doped catalyst with Raman (Fig. S8).

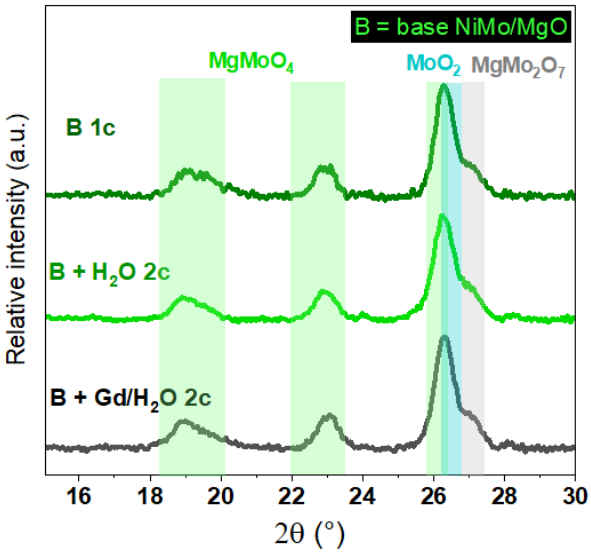

Figure 14. High resolution XRD in the MgMoO4 region of base NiMo/MgO comparison with treatment and Gd addition.

IWI treatment at different stages of the catalyst preparation was evaluated in order to deconvolute the effects of water addition from those of the calcination that is performed after IWI. **Figure 15** presents rate profiles for different treatment stages: (a) the base NiMo/MgO catalyst, (b) water addition without further calcination, (c) two consecutive calcinations without water addition, and (d) water addition with a second calcination. Compared with the untreated catalyst, the addition of water without further calcination (green line) showed a slight enhancement in initial rate. The water addition forms $Mg(OH)_2$ adding hydroxyl groups to the catalyst which would affect Mo reduction, disrupting carburization and carbon nucleation steps leading to the fastest deactivation.

Consecutive calcination without any water introduction (blue line) also achieved its maximum rate earlier and moderated deactivation. A second calcination would promote the active metal sintering [48], however this effect on 5% Ni is small, and after 3 hours, the deactivation profile was similar to the base catalyst. Finally, the water washing coupled with a second

calcination has demonstrated the highest initial rate related to carburization and catalyst activation steps. Inset carbon yields show a consistent trend with activity. The partial solubility of MgO could remove MgO clumps in the surface and expose hindered Ni clusters, while a second calcination would remove water molecules on particles eggshell to promote Ni exposure.

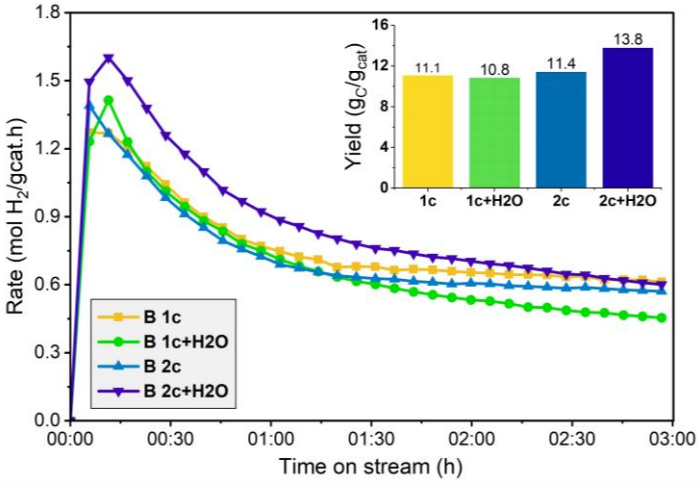

Figure 15. H_2 evolution rate profiles comparison of NiMo/MgO base treated with water after 1 calcination, 2 consecutive calcinations, and water addition between 2 calcinations.

3.5. Water treatment effect on catalyst species evolution: $NiMoO_4$, $MoMgO_4$, Mo_2C

As the catalyst evolves during reaction, Ni and Mo species change to oxides and carbides. This evolution has been studied in previous work of this group [20]. In fresh catalyst (calcined at 600°C), the most predominant species is $MgMoO_4$ and less proportions of NiO_x. In-situ reduced catalyst showed Ni metal with Mo oxides as $NiMoO_7$, and Mo metal, and $MgMoO_x$ species, additional oxides are observed as MoO_{3-x} and MgO, where Mo demonstrated its role as SMSI promoter and disperser. Once CH_4 is introduced, Mo turns into Mo_2C, and Ni will form carbide in less proportion.

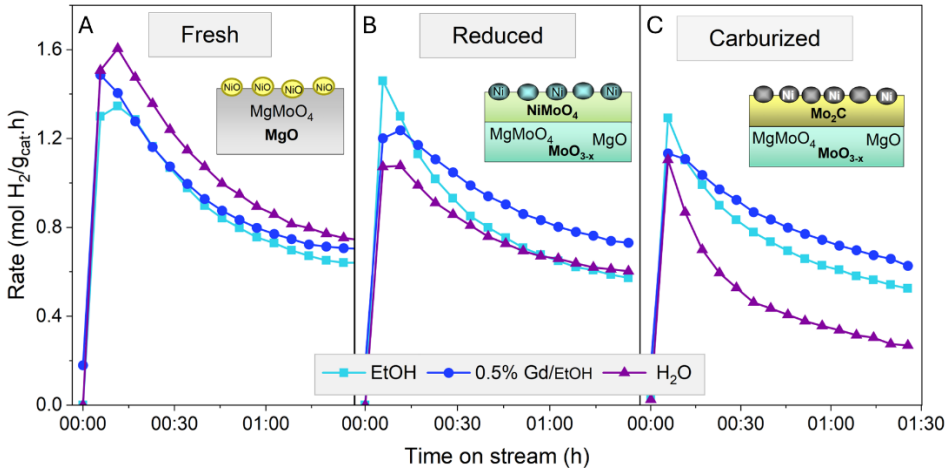

Figure 16. Gd and water addition treatment in prepared catalysts at each stage of NiMo/MgO species evolution. A) Rate evolution of fresh treated catalyst. B) Rate evolution of reduced treated catalyst. C) Rate evolution of carburized treated catalyst.

Gd and water were added after calcination, reduction and carburization in order to identify which species were responsible for higher activity. **Figure 16 A-C** depicts the rate profiles after the catalyst treatment during the catalyst evolution. The Gd precursor addition in all these catalysts tests was done with ethanol to subtract the effect of water. **Figure 16A** shows the solvent effects on rate profiles: a comparison of water and ethanol addition on the base NiMo/MgO catalyst, as well as Gd addition with ethanol. Water treatment showed higher activity compared to ethanol-added-base. Base prepared with ethanol had similar profiles as non-addition (Fig. S9). However, the Gd addition with ethanol evidence the poor effect of Gd to boost CH_4 activation over NiMo/MgO. Although previous work in Gd showed significant positive effects [41], the SMSI between Ni and Mo can hinder any dopant effect. These observations restate that the rate boost is mostly due to water with a second calcination treatment.

Figure 16B shows the profiles for Gd addition in ethanol and water treatment in ex-situ reduced catalyst upon $NiMoO_4$ presence. The post-calcination after solvents addition strongly

deactivated the catalyst (Fig. S10), deactivation is less pronounced with only one calcination. It will also oxidize reduced Mo species formed. In both cases, water decreased the activity compared with ethanol addition. Gd doped catalyst showed a decrease in carburization and activation steps but a prolonged lifetime. These results imply that water treatment is detrimental on $NiMoO_4$.

XRD analysis on reduced samples shows that water introduces OH groups in $Mg(OH)_2$ formation (Fig. S11). We hypothesize that upon reduction, OH groups would promote Mo oxides rather than $MgMoO_4$, disrupting carburization and Ni exsolution. The solvents effect on carburized catalysts, by 5 min exposure to methane, is shown in **Figure 16C**, evaluated with one calcination only because double one would oxidize and burn carbon species formed. A great decrease in the overall rate plus strong deactivation for water treatment is observed compared with ethanol addition. In the same plot, Gd added with ethanol exhibits less decrease in the overall rate and slight inhibition of the carburization step. Mo_2C species were more prone to deactivation with water. From the by-stage analysis, the species responsible for higher rates is the water treatment plus second calcination of $MgMoO_4$.

It was found high solubility of $MgMoO_4$ in water: 14g per 100 ml of water at 22°C [45]. Once water drops are added by IWI, water could be altering the lattice of $MgMoO_4$ oxides introducing O species that make the catalyst more active. Or either, it can promote the washing effect of $MgMoO_4$ by making more Ni available for CH_4 activation. XDR analysis at fresh stage have shown that the bulk structure of $MgMoO_4$ remains the same after Gd and IWI treatment with water, so the changes are expected at the surface. In that sense, the pH of diluted MgO was 8.2, corresponding to a basic environment that promotes MoO_4^{2-} ion formation according to Pourbaix diagram (Fig. S12). These results point out that dissolution of MgO and $MgMoO_4$ plays a big role in the distribution of Ni, Mo and MgO.

3.4. Surface changes upon water-induced metal exposure

To test surface changes, ex situ XPS analysis was conducted over base and water-treated catalysts to identify surface differences, where Ni, Mo, and Mg spectra were tracked. Complete sets of XPS spectrum are shown in Fig. S13, and binding energies are displayed in Tables S2. The elemental analysis found that the Ni content was higher for treated samples (Fig. S14), higher Ni content is also observed by EDS analysis (Table S3). The trend is consistent through fresh and reduced catalysts; upon carburization, Ni proportions were similar when carbon filled the surface and noisy signal in Ni was captured (Fig. S15). **Figure 17** shows the comparison of Ni/Mo ratios throughout catalyst evolution stages, where Ni showed higher abundance respect to Mo in water-treated catalysts than base for all stages.

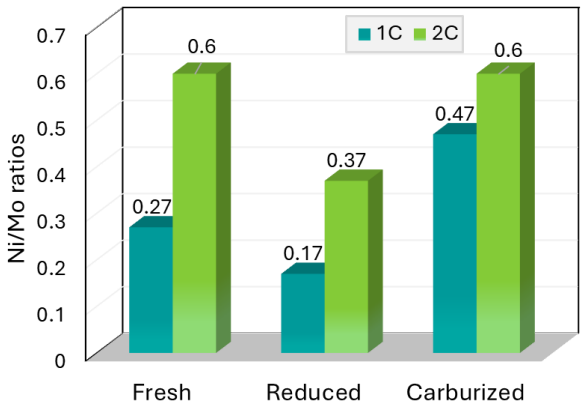

Figure 17. Elemental composition based on high resolution XPS of Ni and Mo content on the surface during catalyst evolution of NiMo/MgO.

Water treatment exhibits the highest Ni/Mo ratio, 122% higher than the base in fresh catalyst, while base catalyst shows its highest during carburization step. The Ni exsolution process in base catalyst surge upon carburization, reaching 176% increase in NiMo ratio from reduction to carburization step, in contrast, treated catalyst had more Ni clusters exsolved in fresh production, lowering after reduction but exposed again in carburization.

Higher Ni/Mo ratios at the outer surface are the main reason for higher activity of IWI treated catalyst. Therefore, effect of Gd is perceived when more Ni is exposed, producing either electronic or geometrical effects. Higher Ni exposure after water washing plus second calcination is related to the partial solubility of MgO and $MgMoO_4$ oxides occurring upon water addition. Such structure is consolidated with a second calcination, eliminating hydroxyl species of the lattice. The partial dissolution would free and clean covered Ni cluster from uppermost bundles of MgO and $MgMoO_4$.

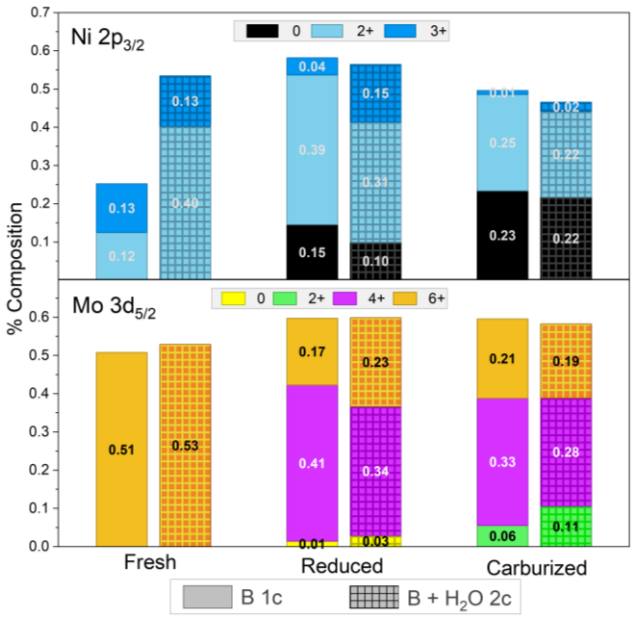

Figure 18. Oxidation states of Ni $2p_{3/2}$ and Mo $3d_{5/2}$ evolution after calcination, reduction and carburization for base and treated NiMo/MgO.

Figure 18 shows the changes of oxidation state (OS) for base and treated NiMo/MgO focused on Ni 2p and Mo 3d regions. Complete Ni OS evolution is shown in Fig. S15. **Figure 19** shows the nickel $2p_{3/2}$ region of fresh catalyst, where Ni^{2+} species content doubles on treated catalyst than the base. Ni^{2+} is associated with NiO and $NiMoO_4$ alloy [20], while Ni^{3+} comprises Ni_2O_3, representing for both cases only 13% of total Ni in **Figure 18**. Ni^0 appears upon reduction

by 851.6 eV, and represent the main active sites. We hypothesize 2+ oxidation state will lead to reduction into 0, and part will remain with Mo alloy. After reduction, higher Ni^0/Ni^{2+} ratio was found on base catalyst, while treated catalyst kept Ni^{2+} predominance, maintaining Ni-Mo bonds (correlated with Mo^{6+}). Once carburization happens, after reduction, carbide formation tends to disrupt Ni-Mo bond, and Ni^0 exsolves forming new active sites. Ni^0/Ni^{2+} ratio increased around 150% and 200% for base and treated catalyst respectively. These changes towards the carburization process, implies higher exsolution of new Ni sites and Mo carburization of $NiMoO_4$ species, as observed with Ni/Mo ratios (**Figure *17***).

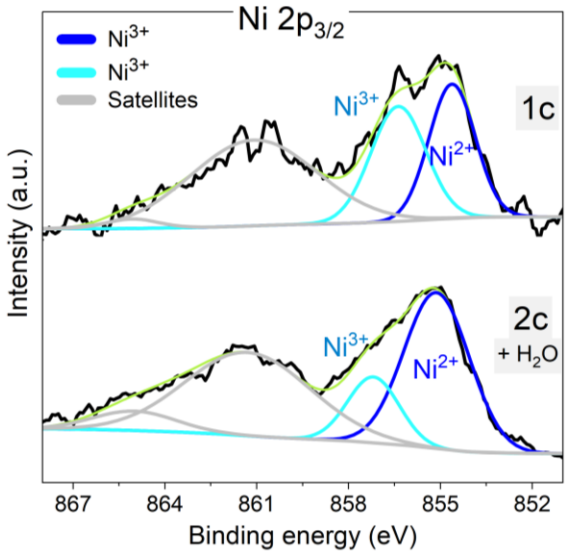

Figure 19. XPS spectra of region Ni $2p_{3/2}$ in fresh catalyst.

Molybdenum 3d region doublet peaks of Mo $3d_{5/2}$ and Mo $3d_{3/2}$ bands in fresh, reduced and carburized catalysts are displayed in Fig. S16. OS are consistent for both doublet regions (Fig. S17). Fresh catalyst showed only Mo^{6+} composition in both catalysts in **Figure 18**. Mo^{6+} is related to $MgMoO_4$ and $NiMoO_4$ alloys. Upon reduction at 650°C, Mo^0 and Mo^{4+} appeared as part of Mo^{6+} reduction, where Mo^{4+} is related to MoO_2 species, being inert for catalysis [49]. Around 20% of Mo^{6+} remained as alloys and oxides, which correlates with remained Ni^{2+} of $NiMoO_4$ formation.

Almost 41% of Mo^{6+} were reduced to Mo^{4+} in the base, and 34% were reduced in treated catalyst, while 1to 3% of Mo was overreduced to Mo^{0}. After carburization, Mo^{2+} species associated to carbide formation [20], had 93% more abundance on treated samples as shown in **Figure 20**. Mo^{6+} still kept on the surface in both cases, and Mo^{2+}/Mo^{4+} ratios were 105% higher in the catalyst treated than base, which aligns with observation of Ni sites increase, implying higher carburization and Ni exsolution.

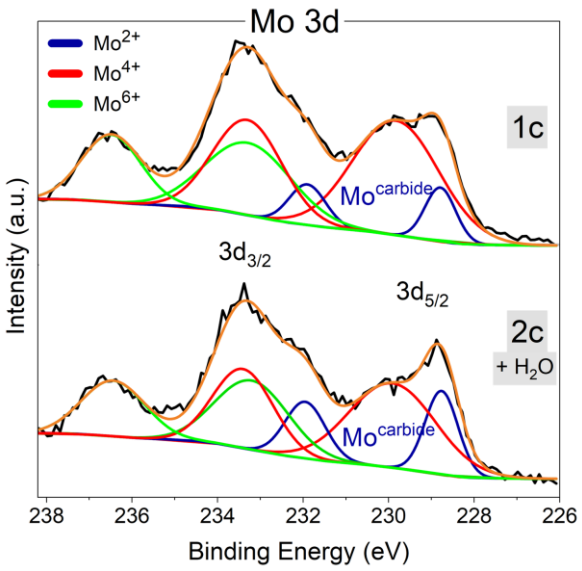

Figure 20. Region Mo 3d of carburized catalyst; for base and treated NiMo/MgO catalyst.

3.5. Evaluation of carbon products

The effect of surface differences of treated catalyst on carbon production, mostly as CNTs, was analyzed by Raman and TEM. Raman showed the graphitic quality of CNTs, while TEM displayed the diameter distribution of the CNTs as well as its morphology.

Raman analysis was used to evaluate the degree of graphitization based on the relative ratio of D to G band. The D band at 1340 cm^{-1} is attributed to structural disorder or defects within the graphite lattice in CNTs or other carbon forms, while the G band, observed at 1585 cm^{-1}, arises from the in-plane stretching vibrations of sp^2 hybridized C-C bonds. The relative D/G ratio expresses the graphitization of CNTs and degree of disorder in the structure, related to the quality of CNTs [50]. CNTs produced by base and treated catalyst, show D/G ratios in the range 0.77 to 1.16 respectively, as displayed in **Figure 21A**. The water washing treatment demonstrated to lower significantly the D/G ratio by 9%, according with t test. **Figure 21B** shows the Raman spectra of one set of samples, G band height and area increased respect to D band in treated samples. Higher amounts of defective carbon can be related with low Ni/Mo ratios as assessed by Pan et al. [51], demonstrating that increasing Mo favors the carbon productivity but more defective and higher CNTs diameter is observed [18].

As we see later, the CNT diameter decreased with water treatment, which increased the graphitic quality. The carbon production was compared over time of reaction in **Figure 21C**. After 3 hours, the defective carbon of the base catalyst increases, while treated samples maintain the graphitic nature. This implies that the deactivation decay (k_d) observed in treated samples is not necessarily due to higher coke formation, instead, an encapsulation and metal lost in CNTs is likely.

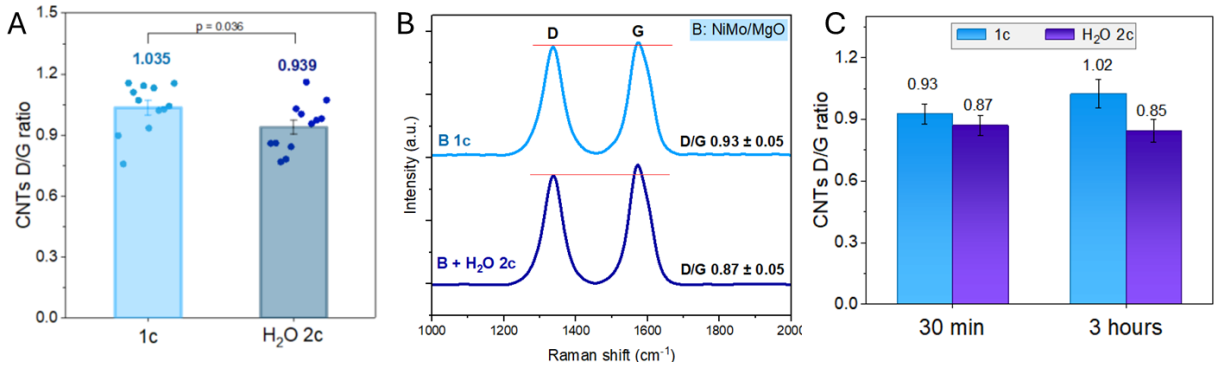

Figure 21. Raman analysis of CNTs. a) D/G ratio analyzed with t test in treated catalyst respect to the base, b) D and G bands of base and treated CNTs, c) D/G ratios at 30 min and 3 hours of time on stream.

The increase of Ni exposure on treated samples can lead to better surface structure and dispersion. From this, analysis of multi-wall carbon nanotubes (MWCNTs) produced was made by TEM and it is shown in **Figure 22**, where the diameter distribution was assessed. The comparison of diameter distribution on base and treated samples was made upon 228 counts. A reduction in the average diameter is observed: base NiMo/MgO had an average of 12.2 nm, while treated catalyst lower the size to 10.8 nm. This trend agrees with D/G ratio of Raman, since less defective carbon is related to lower diameter size and number of walls [51]. The measured diameters in both catalysts presented broad distributions with thin and thick tubes (Fig. S18). Some works have reported that CNTs produced by CH_4 present broader distributions on size due to H_2 effects compared with C-O species [52]. Hydrogen may adsorb on the catalyst surface, affecting the catalytic behavior, and may also etch carbon species including amorphous and graphitic carbon [25].

Figure 22A shows a broader distribution for the base catalyst, which reflects a frequent morphology of entangled CNTs that results into high average diameter, as illustrated in **Figure 22B**. Base catalyst presents less Ni exposure, which would be more influenced by the effects of

Mo and H_2, disrupting carbon nucleation and leading to an early tube entanglement and defect formation. **Figure 22C** shows a sharper distribution in treated catalysts, whose morphology is more uniform in **Figure 22D** and Fig. S19. The treatment shifted the average CNTs size towards lower diameter (it triples the 7 nm frequency) due to lack of entangled CNTs, since 11.5 and 13.5 nm were the most counted diameter for base and treated cases. This effect could be explained by higher Ni clusters exposure in the surface with low coordination numbers, leading to more dispersion, and lower particle size. The lower diameter for treated catalyst was consistent after 3 hours of reaction as shown by Fig. S20. This agrees with Raman D/G ratio also after 3 hours, so the reaction deactivates principally by metal lost in the construction of a MWCNT. The entangled CNTs present more defects in its structure with apparent change of elongation angle [53].

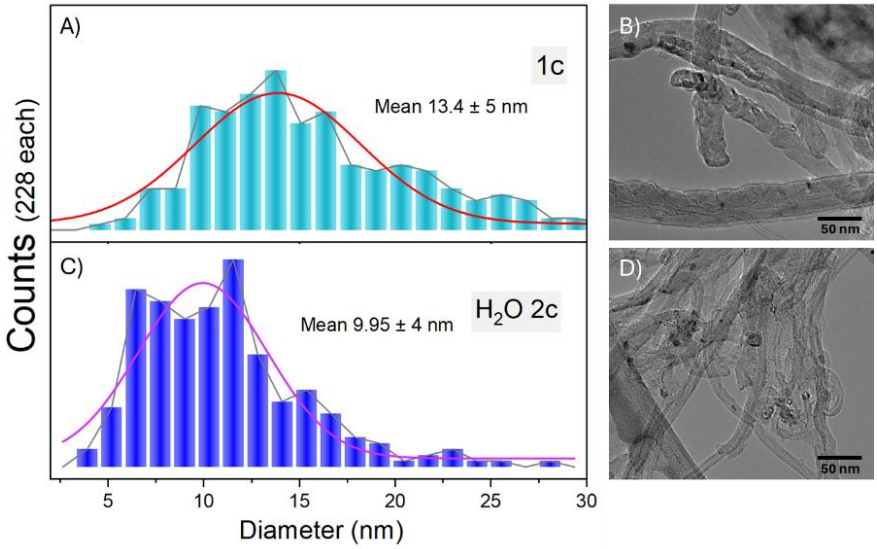

Figure 22. Diameter distribution and HR-TEM images of CNTs produced from base and water treated NiMo/MgO at 800°C.

3.6. Mechanistic insight into water-induced metal exposure

Combining the experiment results of catalytic activity of treated NiMo/MgO and catalyst characterization, **Figure 23** summarizes the overall dynamics on the surface. The Ni exposure

process upon water addition proceeded through an initial $MoMgO_4$ dissolution on water, leading to surface washing as **Figure 23A**. Washing process exposes NiO nanoparticles and $NiMoO_4$ species on the surface. After drying, remaining OH groups of formed $Mg(OH)_2$ are removed by the second calcination, stabilizing the exposed Ni clusters at the surface. The subsequent in situ reduction removes some oxygen in oxide lattices and creates metallic Ni clusters as main active sites. Once carburization takes place via methane introduction, $NiMoO_4$ species are dissociated to form Mo_2C and separated Ni comprise secondary sites for methane activation and carbon nucleation. The treatment promotes Ni clusters exposure and increases Ni exsolution through higher carburization of $NiMoO_4$ species. On a metallic surface, the Gd dopant effect on Ni can be better described by rate profiles.

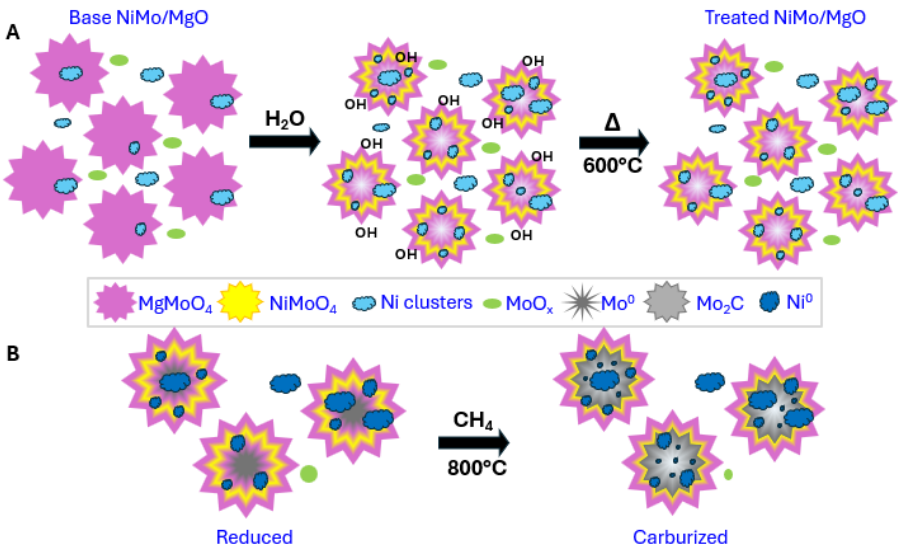

Figure 23. Schematic of (A) formation of Ni nanoparticles clusters during IWI treatment, and (B) carburization and Ni exsolution mechanism upon methane introduction.

Chapter 4: Concluding remarks

The present study provides new mechanistic and practical insights into the role of dopants in the highly dynamic NiMo/MgO for H_2 and CNT production from CMD. We found that IWI method is more efficient for dopant addition, and from tested dopants, Gd shows a modest positive effect in NiMo/MgO, however, the effect of Mo can hinder its effects. IWI treatment not only highlights dopant effects but also the role of water in restructuring surface species and promoting Ni exposure after a second calcination. Induced metal exposure distributed along catalyst particles achieved an optimal initial rate in hydrogen production, boosting 30% of the initial activity and yielding 14.3 g_{CNT}/g_{cat} (14% higher than base) during CMD. Besides, washing of $MgMoO_4$ and higher $NiMoO_4$ formation are the main phases associated with metal Ni exposure and higher carburization mechanisms. The characterization of CNTs produced implies that an increase on Ni distribution over the surface upon carburization significantly influenced the nucleation process. Treated samples enhanced graphitic carbon formation and narrowed the distribution of CNTs. The wetness impregnation treatment induced Ni metal exposure on particulate catalyst, promoting slight Gd positive effects on rates. These findings advance the understanding of highly dynamic catalysts for high-yield CMD processes, providing a meaningful reference to further development in doped catalyst preparation.

5. References

1. Bank, W., *Global Gas Flaring Tracker Report*, W.B. Publications, Editor. 2025, World Bank: Washington.
2. Leung, S.L., et al., *Dynamics and Mechanism of Carbon Filament Formation during Methane Reforming on Supported Nickel Clusters.* The Journal of Physical Chemistry C, 2020. **124**(37): p. 20143-20160.
3. Sánchez-Bastardo, N., R. Schlögl, and H. Ruland, *Methane Pyrolysis for Zero-Emission Hydrogen Production: A Potential Bridge Technology from Fossil Fuels to a Renewable and Sustainable Hydrogen Economy.* Industrial & Engineering Chemistry Research, 2021. **60**(32): p. 11855-11881.
4. Snoeck, J.W., G.F. Froment, and M. Fowles, *Kinetic Study of the Carbon Filament Formation by Methane Cracking on a Nickel Catalyst.* Journal of Catalysis, 1997. **169**(1): p. 250-262.
5. Ding, L.P., et al., *Why Carbon Nanotubes Grow.* Journal of the American Chemical Society, 2022. **144**(12): p. 5606-5613.
6. Snoeck, J.W., G.F. Froment, and M. Fowles, *Filamentous Carbon Formation and Gasification: Thermodynamics, Driving Force, Nucleation, and Steady-State Growth.* Journal of Catalysis, 1997. **169**(1): p. 240-249.
7. Awadallah, A.E., et al., *Catalytic Decomposition of Natural Gas to CO/CO2-Free Hydrogen Production and Carbon Nanomaterials Using MgO-Supported Monometallic Iron Family Catalysts.* Chemical Engineering Communications, 2015. **202**(2): p. 163-174.
8. Pudukudy, M. and Z. Yaakob, *Methane decomposition over Ni, Co and Fe based monometallic catalysts supported on sol gel derived SiO2 microflakes.* Chemical Engineering Journal, 2015. **262**: p. 1009-1021.
9. Saconsint, S., et al., *Development of high-performance nickel-based catalysts for production of hydrogen and carbon nanotubes from biogas.* Scientific Reports, 2022. **12**(1): p. 15195.
10. Awadallah, A.E., et al., *Catalytic thermal decomposition of methane to COx-free hydrogen and carbon nanotubes over MgO supported bimetallic group VIII catalysts.* Applied Surface Science, 2014. **296**: p. 100-107.

11. Dong, H., et al., *Pyrolysis gas from biomass and plastics over X-Mo@MgO (X = Ni, Fe, Co) catalysts into functional carbon nanocomposite: Gas reforming reaction and proper process mechanisms.* Science of The Total Environment, 2022. **831**: p. 154751.
12. Cassell, A.M., et al., *Large Scale CVD Synthesis of Single-Walled Carbon Nanotubes.* The Journal of Physical Chemistry B, 1999. **103**(31): p. 6484-6492.
13. Wang, I.W., et al., *Methane Pyrolysis for Carbon Nanotubes and COx-Free H2 over Transition-Metal Catalysts.* Energy & Fuels, 2019. **33**(1): p. 197-205.
14. Horváth, A., et al., *Methane pyrolysis on NiMo/MgO catalysts: The significance of equimolar NiMo alloy resisting nanosize segregation during the reaction.* Applied Catalysis A: General, 2024. **676**: p. 119651.
15. Awadallah, A.E., et al., *Influence of Mo or Cu doping in Fe/MgO catalyst for synthesis of single-walled carbon nanotubes by catalytic chemical vapor deposition of methane.* Fullerenes, Nanotubes and Carbon Nanostructures, 2017. **25**(4): p. 256-264.
16. Aboul-Enein, A.A. and A.E. Awadallah, *Impact of Co/Mo ratio on the activity of CoMo/MgO catalyst for production of high-quality multi-walled carbon nanotubes from polyethylene waste.* Materials Chemistry and Physics, 2019. **238**: p. 121879.
17. Awadallah, A.E., A.A. Aboul-Enein, and A.K. Aboul-Gheit, *Impact of group VI metals addition to Co/MgO catalyst for non-oxidative decomposition of methane into COx-free hydrogen and carbon nanotubes.* Fuel, 2014. **129**: p. 27-36.
18. Zhou, L.-P., et al., *Catalytic Functions of Mo/Ni/MgO in the Synthesis of Thin Carbon Nanotubes.* The Journal of Physical Chemistry B, 2005. **109**(10): p. 4439-4447.
19. Zhang, X., et al., *Evolution of catalyst design for controlled synthesis of chiral single-walled carbon nanotubes.* Chemical Communications, 2024. **60**(49): p. 6222-6238.
20. Gomez, L.A., et al., *Evolution of Ni-Mo/MgO during catalytic methane pyrolysis to produce base-growth nanotubes.* Cell Reports Physical Science, 2025. **6**(4): p. 102519.
21. Li, Y., et al., *Single phase MgMoO4 as catalyst for the synthesis of bundled multi-wall carbon nanotubes by CVD.* Carbon, 2005. **43**(6): p. 1325-1328.
22. Monzon, A., et al., *Kinetic modeling of the SWNT growth by CO disproportionation on CoMo catalysts.* J Nanosci Nanotechnol, 2008. **8**(11): p. 6141-52.

23. Park, S.J., et al., *Effect of reduction conditions of Mo-Fe/MgO on the formation of carbon nanotube in catalytic methane decomposition.* Journal of Industrial and Engineering Chemistry, 2022. **109**: p. 384-396.
24. Zheng, J., et al., *Mo promoting Ni-based catalysts confined by halloysite nanotubes for dry reforming of methane: Insight of coking and H2S poisoning resistance.* Applied Catalysis B: Environmental, 2024. **342**: p. 123369.
25. Lolli, G., et al., *Tailoring (n,m) Structure of Single-Walled Carbon Nanotubes by Modifying Reaction Conditions and the Nature of the Support of CoMo Catalysts.* The Journal of Physical Chemistry B, 2006. **110**(5): p. 2108-2115.
26. Pan, Z., et al., *Tunable synthesis of carbon nanotubes via methane catalytic pyrolysis by adjusting Mo incorporation in Fe/MgO.* Physical Chemistry Chemical Physics, 2025. **27**(35): p. 18302-18308.
27. Nakaya, Y. and S. Furukawa, *Catalysis of Alloys: Classification, Principles, and Design for a Variety of Materials and Reactions.* Chemical Reviews, 2023. **123**(9): p. 5859-5947.
28. Nakaya, Y., et al., *Single-atom Pt in intermetallics as an ultrastable and selective catalyst for propane dehydrogenation.* Nature Communications, 2020. **11**(1): p. 2838.
29. Zhu, H., et al., *Sn surface-enriched Pt–Sn bimetallic nanoparticles as a selective and stable catalyst for propane dehydrogenation.* Journal of Catalysis, 2014. **320**: p. 52-62.
30. Lang, Z., et al., *A Mini-Review on Hydrogen and Carbon Production from Methane Pyrolysis by Molten Media.* Energy & Fuels, 2024. **38**(24): p. 23175-23191.
31. Fei, J., et al., *Doped Ni Catalysts for Methane Reforming with CO2.* Catalysis Letters, 2004. **98**(4): p. 241-246.
32. Li, W., et al., *Bi-reforming of model biogas into syngas over layered double hydroxides-derived bimetallic Ni-Ga catalysts.* Fuel, 2024. **369**: p. 131792.
33. Herrera, J.E. and D.E. Resasco, *Loss of single-walled carbon nanotubes selectivity by disruption of the Co–Mo interaction in the catalyst.* Journal of Catalysis, 2004. **221**(2): p. 354-364.
34. Amin, M.H., et al., *Understanding the role of lanthanide promoters on the structure–activity of nanosized Ni/γ-Al2O3 catalysts in carbon dioxide reforming of methane.* Applied Catalysis A: General, 2015. **492**: p. 160-168.

35. Pino, L., et al., *Hydrogen production by methane tri-reforming process over Ni–ceria catalysts: Effect of La-doping.* Applied Catalysis B: Environmental, 2011. **104**(1): p. 64-73.
36. Sarkar, B., et al., *Highly nanodispersed Gd-doped Ni/ZSM-5 catalyst for enhanced carbon-resistant dry reforming of methane.* Journal of Molecular Catalysis A: Chemical, 2016. **424**: p. 17-26.
37. Zhang, M., et al., *Effects of the surface adsorbed oxygen species tuned by rare-earth metal doping on dry reforming of methane over Ni/ZrO2 catalyst.* Applied Catalysis B: Environmental, 2020. **264**: p. 118522.
38. Anjaneyulu, C., et al., *Influence of Rare Earth (La, Pr, Nd, Gd, and Sm) Metals on the Methane Decomposition Activity of Ni–Al Catalysts.* ACS Sustainable Chemistry & Engineering, 2015. **3**(7): p. 1298-1305.
39. Sugime, H., et al., *Ultra-long carbon nanotube forest via in situ supplements of iron and aluminum vapor sources.* Carbon, 2021. **172**: p. 772-780.
40. Cho, W., M. Schulz, and V. Shanov, *Growth and characterization of vertically aligned centimeter long CNT arrays.* Carbon, 2014. **72**: p. 264-273.
41. Sugime, H., et al., *Gd-Enhanced Growth of Multi-Millimeter-Tall Forests of Single-Wall Carbon Nanotubes.* ACS Nano, 2019. **13**(11): p. 13208-13216.
42. McFarland, E.W. and H. Metiu, *Catalysis by Doped Oxides.* Chemical Reviews, 2013. **113**(6): p. 4391-4427.
43. Gardeh, M.G., et al., *Exploring Mechanisms of Hydration and Carbonation of MgO and Mg(OH)2 in Reactive Magnesium Oxide-Based Cements.* The Journal of Physical Chemistry C, 2022. **126**(14): p. 6196-6206.
44. Kaluža, L., et al., *High-activity MgO-supported CoMo hydrodesulfurization catalysts prepared by non-aqueous impregnation.* Applied Catalysis B: Environmental, 2015. **162**: p. 430-436.
45. Zdražil, M., *MgO-supported Mo, CoMo and NiMo sulfide hydrotreating catalysts.* Catalysis Today, 2003. **86**(1): p. 151-171.
46. Munnik, P., P.E. de Jongh, and K.P. de Jong, *Recent Developments in the Synthesis of Supported Catalysts.* Chemical Reviews, 2015. **115**(14): p. 6687-6718.

47. Li, S., et al., *The improvement of yield and thermal stability of single-walled carbon nanotubes fabricated by Gd-assisted FCCVD.* Materials Letters, 2023. **340**: p. 134153.
48. Ren, Z., et al., *Unsupported nickel catalyst prepared from nickel foam for methane decomposition and recycling the carbon deposited spent catalyst.* International Journal of Hydrogen Energy, 2021. **46**(42): p. 21853-21865.
49. Gomez, L.A., et al., *Revealing the Mechanistic Details for the Selective Deoxygenation of Carboxylic Acids over Dynamic MoO3 Catalysts.* ACS Catalysis, 2023. **13**(13): p. 8455-8466.
50. Sierra Gallego, G., et al., *Production of hydrogen and MWCNTs by methane decomposition over catalysts originated from LaNiO3 perovskite.* Catalysis Today, 2010. **149**(3): p. 365-371.
51. Pan, Z., et al., *Tunable synthesis of carbon nanotubes via methane catalytic pyrolysis by adjusting Mo incorporation in Fe/MgO.* Physical Chemistry Chemical Physics, 2025.
52. Yang, F., et al., *Chirality Pure Carbon Nanotubes: Growth, Sorting, and Characterization.* Chemical Reviews, 2020. **120**(5): p. 2693-2758.
53. Hofmann, S., et al., *In situ Observations of Catalyst Dynamics during Surface-Bound Carbon Nanotube Nucleation.* Nano Letters, 2007. **7**(3): p. 602-608.
54. Fayazi, M.R., et al., *Targeted elimination of molybdenum ions from a leaching solution with the ability of radiated grafting GMA-PAN nanofibers.* Scientific Reports, 2024. **14**(1): p. 252.

Appendix A: Supporting information

Supplementary information

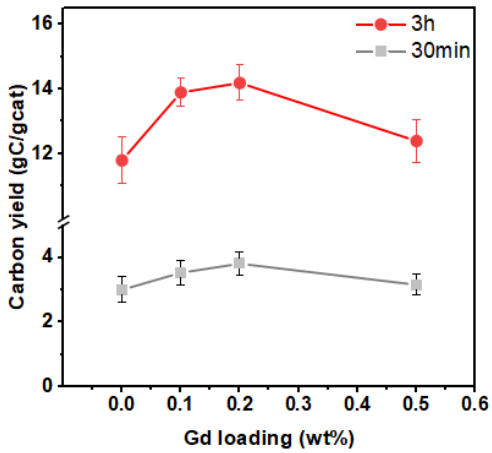

Fig. S1. Carbon yields at lower loadings of Gd at 30 minutes and 3 hours of reaction.

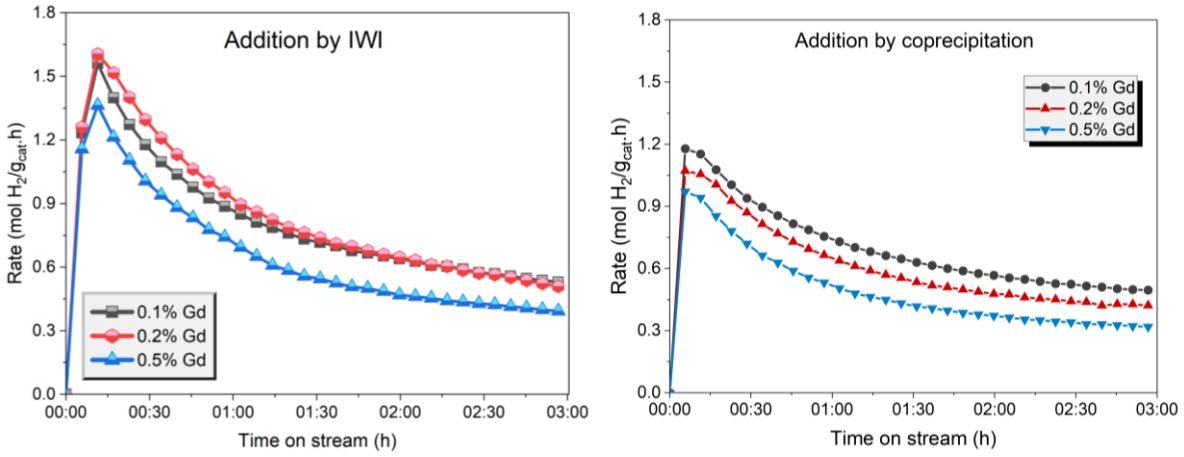

Fig S2. Rate profiles based on H_2 evolution for low Gd loads added by IWI (a) and coprecipitation (b) method.

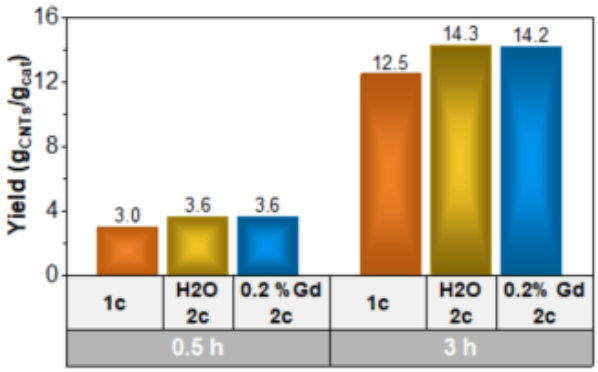

Fig. S3. The carbon accumulations at 0.5 and 3 hours of reaction of base, water-treated and Gd-doped NiMo/MgO catalyst.

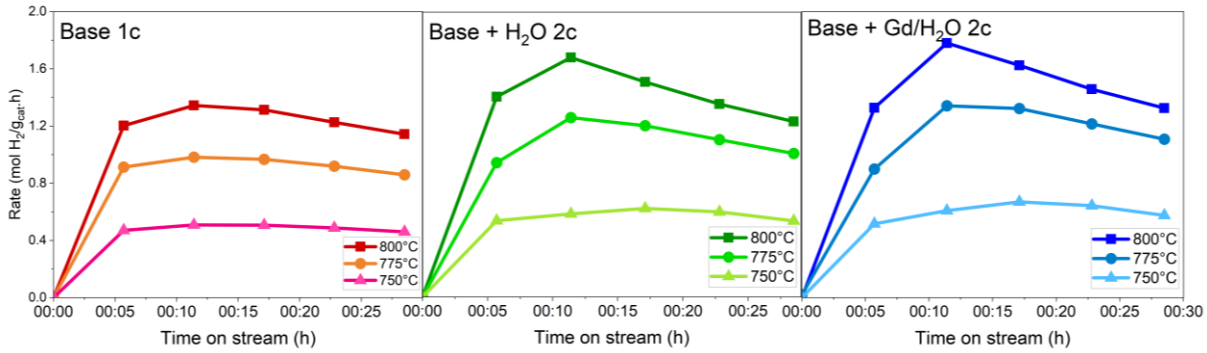

Fig. S4. Temperature dependence of rate profiles based on H_2 evolution by 30 minutes at 800°C.

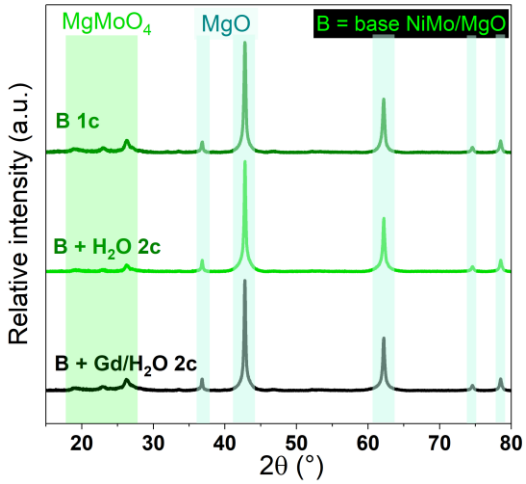

Fig. S6. XRD of NiMo/MgO base, no treated, IWI-treated and Gd added.

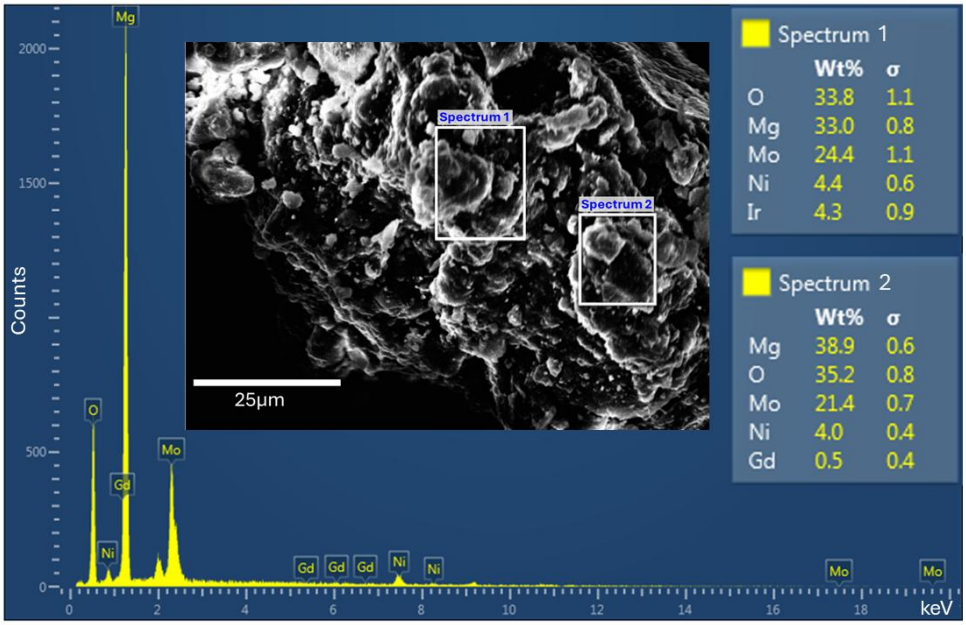

Fig. S7. EDS analysis of 0.2% Gd doped 5%Ni 25%Mo/MgO.

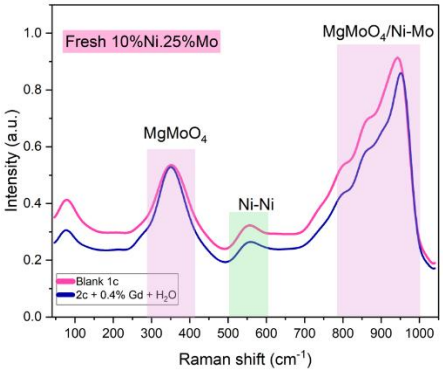

Fig. S8. Raman spectra of base and Gd-doped NiMo MgO catalyst by IWI.

Table S1. Average crystal size (D) of $MgMoO_4$ and $MgMo_2O_7$ species on NiMo/MgO treated catalyst estimated by Scherrer equation. X ray wavelength 1.5406 Å. Shape factor 0.94.

	Specie	D (nm)
1c	$MgMoO_4$	13.1072345
	$MgMo_2O_7$	14.0216934
2c + H2O	$MgMoO_4$	13.9960165
	$MgMo_2O_7$	11.8268304
Gd 2c	$MgMoO_4$	11.9516503
	$MgMo_2O_7$	14.213644

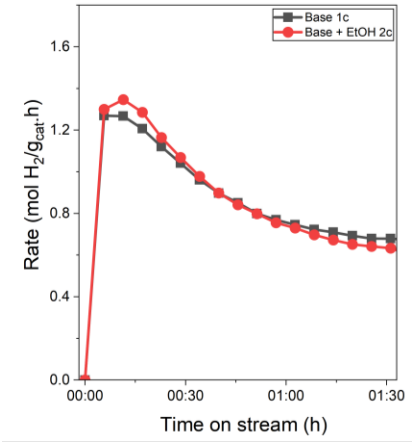

Fig. S9. Rate profiles based on H_2 evolution for base NiMo/MgO and alcohol addition and second calcination treatment.

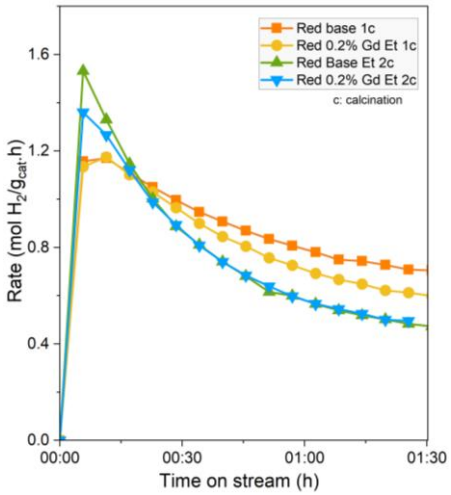

Fig. S10. Rate profiles evaluation for reduced NiMo/MgO with alcohol addition and second calcination treatment.

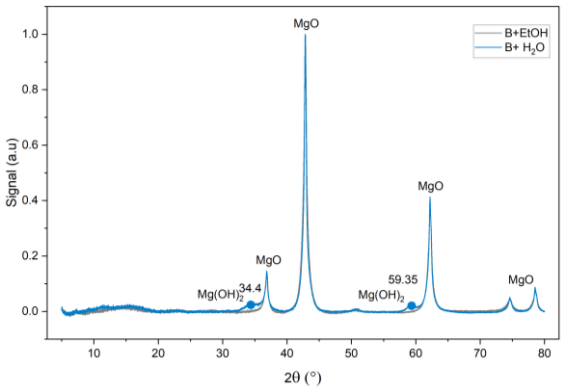

Fig. S11. XRD analysis of reduced NiMo/MgO treated with ethanol and water without second calcination.

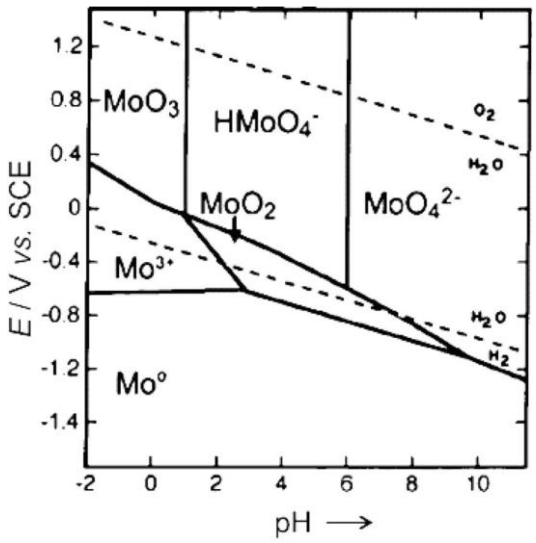

Fig. S12. Pourbaix diagram of molybdenum. Adapted from Fayazi et. al., 2024 [54].

XPS section.

Peaks deconvolution was determined using Origin software with the following constraints: (1) a spin-orbit splitting of 3.15 eV for Mo 3d5/2 and 3d3/2, (2) a spin-orbit splitting of 17.3 eV for Ni 2p3/2 and 2p1/2 and (3) an area ratio of 3:2 for Mo 3d5/2:Mo 3d3/2, and (4) an area ratio of 1:2 for Ni 2p3/2:Ni 2p1/2.

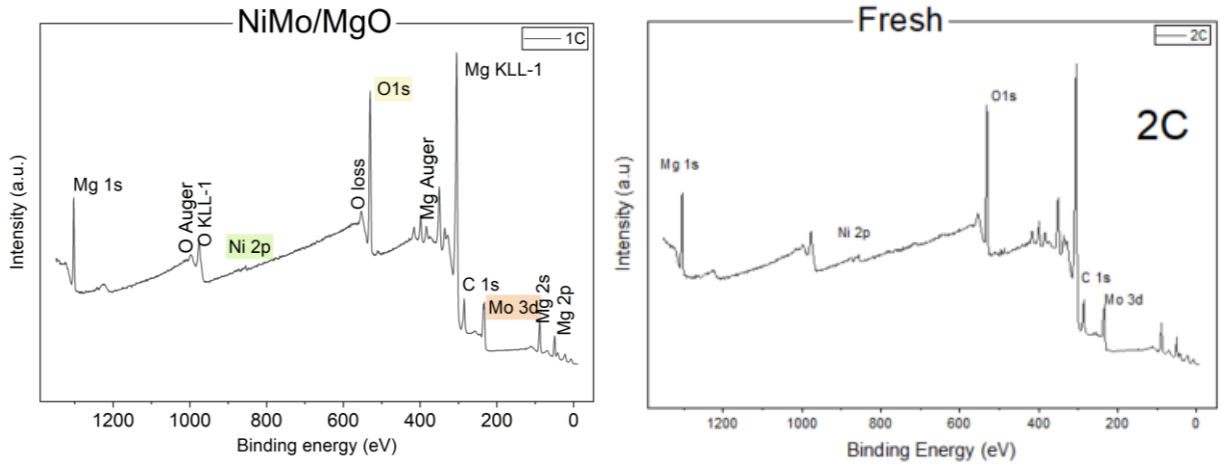

Fig. S13. XPS spectra of fresh base and treated NiMo/MgO.

Tables S2. Binding energies in high resolution regions of Ni and Mo.

a. Binding energy for Ni 2p.

	1C	2C	1C	2C	1C	2C	1C	2C
	Ni 3+		**Ni 2+**		**Ni 0**		**Ni sat**	
Samples	Ni 2p 3/2		Ni 2p 3/2		Ni 2p 3/2		Ni 2p 3/2	
Fresh	856.6	857.1	854.6	855.1	-	-	861	861.3
Reduced	857	856.8	854.8	855.3	852.0	852.4	860.3	861.3
Carburized	857.8	857.5	856.7	856.5	852.8	852.7	861.2	862.2

b. Binding energy for Mo 3d.

	1C	2C	1C	2C	1C	2C	1C	2C
	Mo 6+		**Mo 4+**		**Mo 2+**		**Mo 0**	
Samples	Mo 3d 5/2		Mo 3d 5/2		Mo 3d 5/2		Mo 3d 5/2	
Fresh	232	232.4						
Reduced	232.2	232.6	229.2	229.3			226.9	227.2
Carburized	233.3	233.2	229.8	229.9	228.8	228.8		

	1C	2C	1C	2C	1C	2C	1C	2C
	Mo 6+		**Mo 4+**		**Mo 2+**		**Mo 0**	
Samples	Mo 3d 3/2		Mo 3d 3/2		Mo 3d 3/2		Mo 3d 3/2	
Fresh	234.8	235.4						
Reduced	235.4	235.5	232.4	232.6			230.5	230.5
Carburized	236.5	236.4	233.3	233.4	231.9	232		

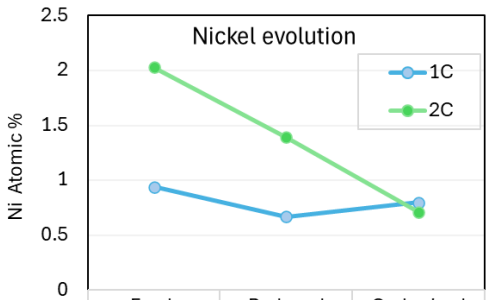

	Fresh	Reduced	Carburized
1C	0.94	0.67	0.8
2C	2.03	1.39	0.71

Fig S14. Elemental analysis percentages for Ni content in XPS.

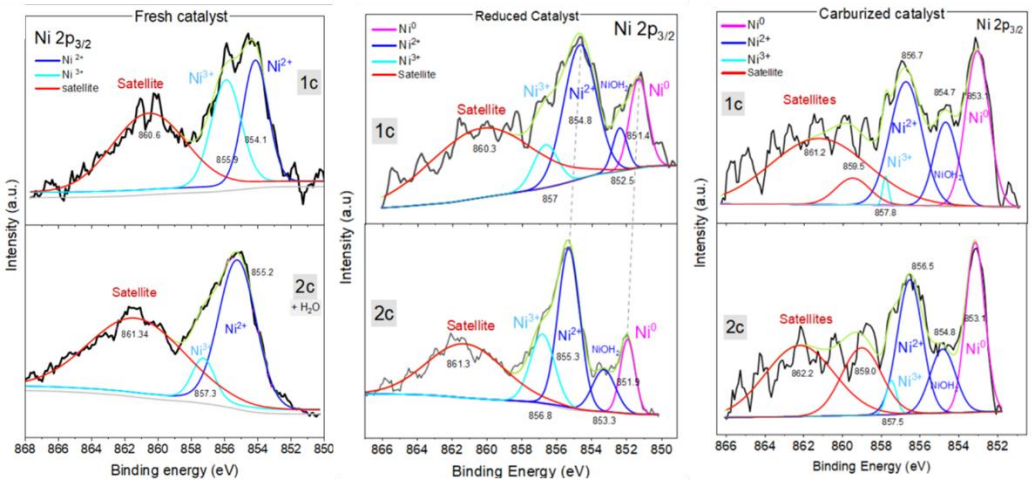

Fig. S15. High resolution XPS spectra of Ni 2p for base and treated catalyst during fresh, reduced and carbonized stages.

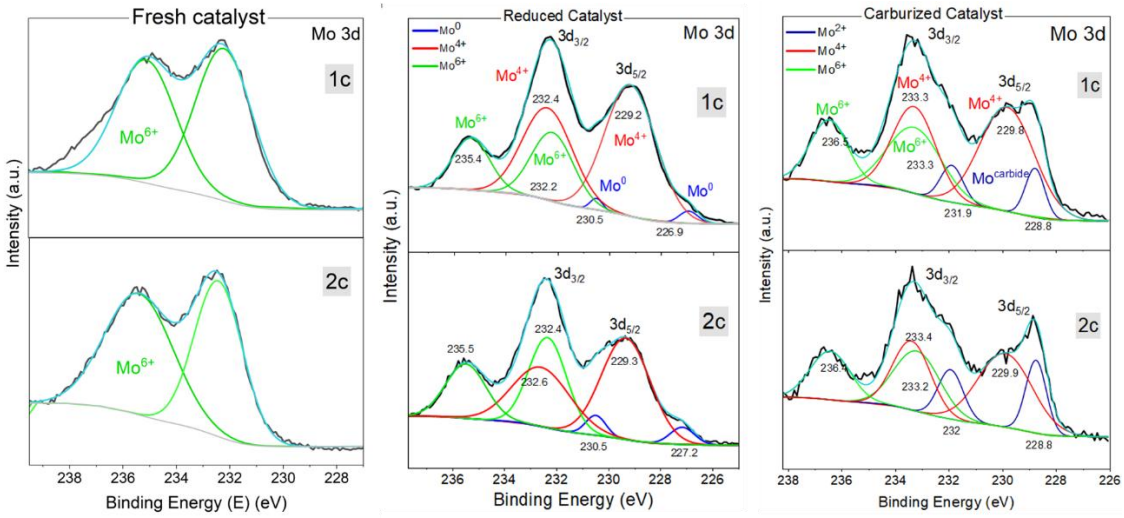

Fig. S16. High resolution XPS spectra of Mo 3d in 3/2 and 5/2 regions during catalyst evolution of NiMo/MgO for base and treated catalyst.

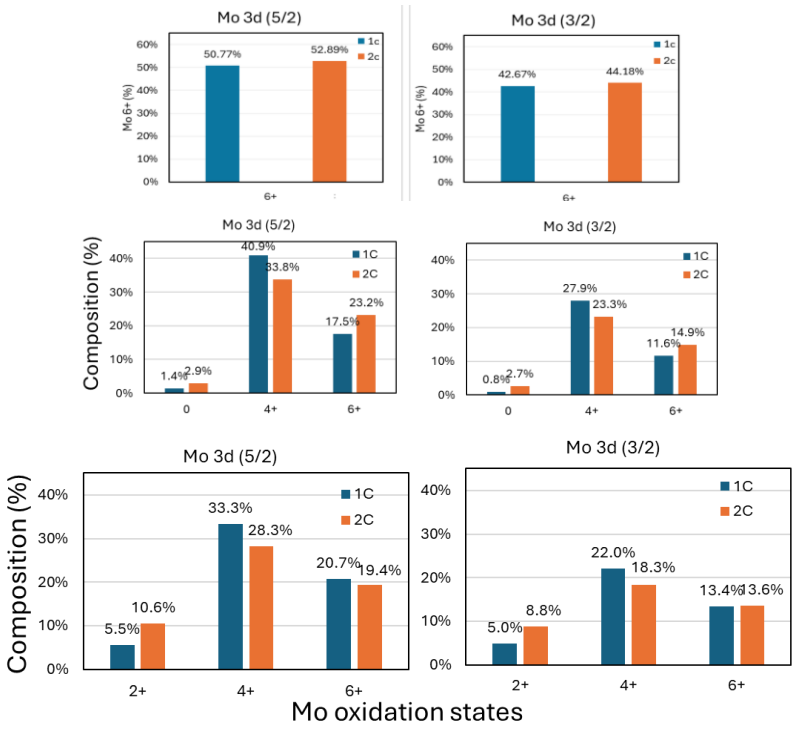

Fig. S17. Oxidation state percentage on Mo 3d doublets region.

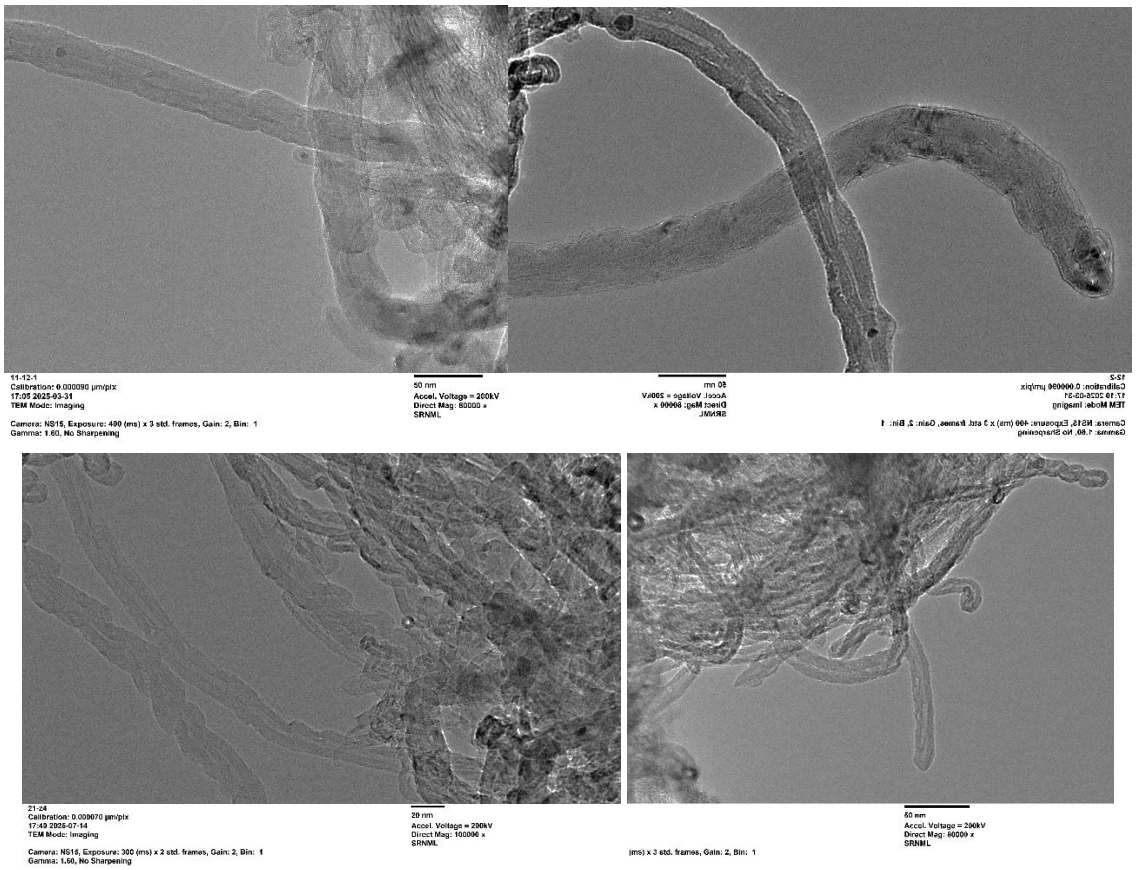

Fig. S18. TEM images of CNTs produced by base NiMo/MgO.

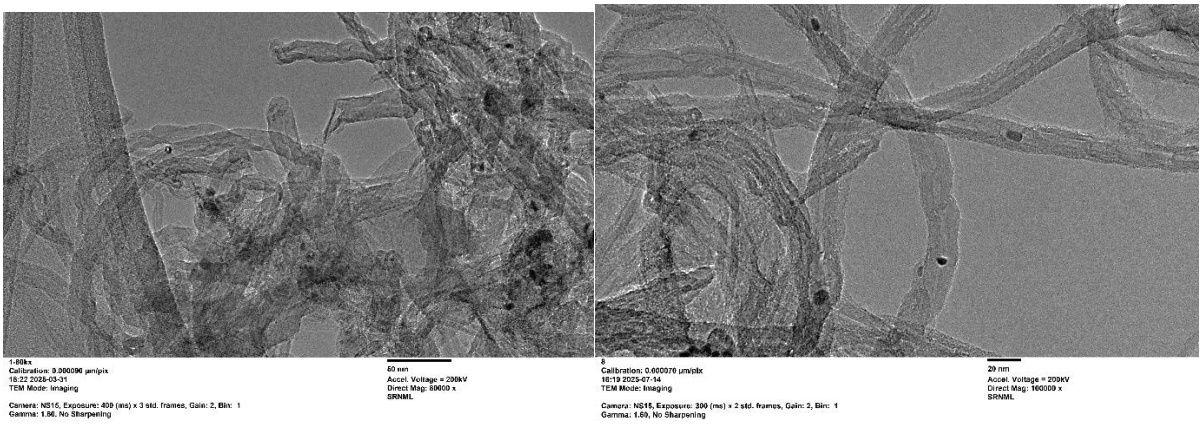

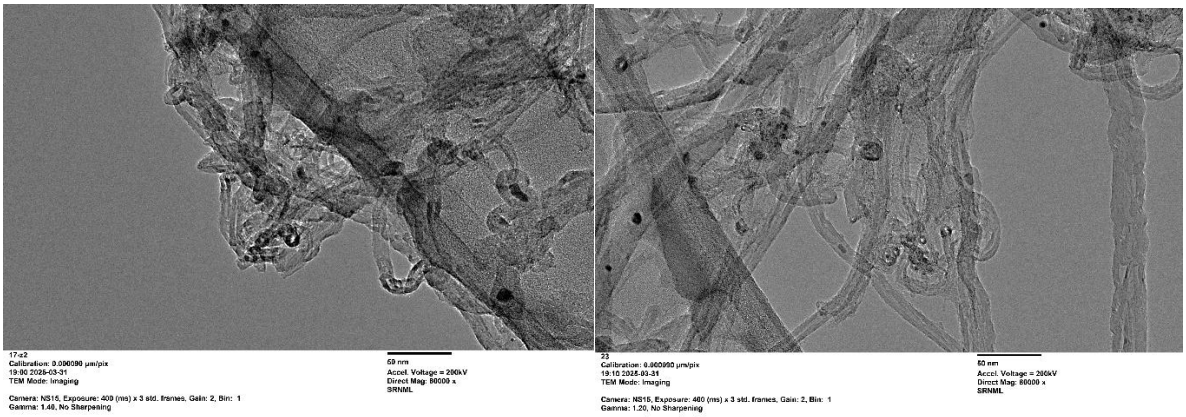

Fig. S19. TEM images of CNTs produced by treated NiMo/MgO.

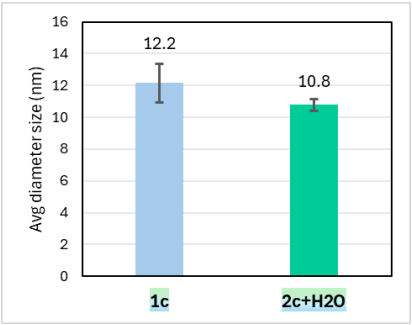

Fig. S20. Mean diameter size after 3h of reaction (200 counts).